JCI The Journal of Clinical Investigation

Neuron-oligodendrocyte potassium shuttling at nodes of Ranvier protects against inflammatory demyelination

Hannah Kapell, … , Sven G. Meuth, Lucas Schirmer

J Clin Invest. 2023. https://doi.org/10.1172/JCI164223.

Research In-Press Preview **Inflammation** **Neuroscience**

Graphical abstract

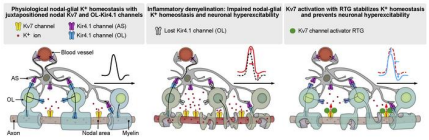

Neuron-oligodendrocyte potassium shuttling at nodes of Ranvier protects against inflammatory demyelination

Hannah Kapell†,[1], Luca Fazio†,[2,3], Julia Dyckow†,[1], Sophia Schwarz[1], Andrés Cruz-Herranz[4], Joaquin Campos[5], Christina Mayer[6], Elisa D´Este[7], Wiebke Möbius[8,9], Christian Cordano[4], Anne-Katrin Pröbstel[4,10], Marjan Gharagozloo[11], Amel Zulji[1], Venu Narayanan Naik[2], Anna Delank[2], Manuela Cerina[2], Thomas Müntefering[3], Celia Lerma-Martin[1], Jana K. Sonner[6], Jung Hyung Sin[4], Paul Disse[12,13], Nicole Rychlik[13, 26], Khalida Sabeur[14,15], Manideep Chavali[14,15], Rajneesh Srivastava[16], Matthias Heidenreich[17], Kathryn C. Fitzgerald[11], Guiscard Seebohm[12], Christine Stadelmann[8,18], Bernhard Hemmer[16,19], Michael Platten[1,20,21,22], Thomas J. Jentsch[17,23], Maren Engelhardt[22,24,25], Thomas Budde[26], Klaus-Armin Nave[8], Peter A. Calabresi[11], Manuel A. Friese[6], Ari J. Green[4,27], Claudio Acuna[5], David H. Rowitch*,[14,15,28,29,30], Sven G. Meuth*,[2,3], Lucas Schirmer*,[1,21,22]

[1]Department of Neurology, Medical Faculty Mannheim, Heidelberg University, Germany.

[2]Department of Neurology with Institute of Translational Neurology, University Hospital Münster, Germany.

[3]Department of Neurology, University of Düsseldorf, Germany.

[4]Weill Institute for Neurosciences, Department of Neurology, University of California San Francisco, USA.

[5]Chica and Heinz Schaller Research Group, Institute of Anatomy and Cell Biology, Heidelberg University, Germany.

[6]Institute of Neuroimmunology and Multiple Sclerosis, Center for Molecular Neurobiology Hamburg, University Medical Center Hamburg-Eppendorf, Germany.

[7]Optical Microscopy Facility, Max Planck Institute for Medical Research, Heidelberg, Germany.

[8]Electron Microscopy Core Unit, Department of Neurogenetics, Max Planck Institute of Experimental Medicine, Göttingen, Germany.

[9]Cluster of Excellence „Multiscale Bioimaging: from Molecular Machines to Network of Excitable Cells“ (MBExC), University of Göttingen, Germany.

[10]Neurologic Clinic and Policlinic and Research Center for Clinical Neuroimmunology and Neuroscience Basel, Departments of Medicine, Biomedicine, and Clinical Research, University Hospital of Basel, University of Basel, Switzerland.

[11]Departments of Neurology and Neuroscience, Johns Hopkins University School of Medicine, Baltimore, USA.

[12]Institute for Genetics of Heart Diseases (IfGH), Cellular Electrophysiology and Molecular Biology, University Hospital Münster, Münster, Germany.

[13]University of Münster, Chembion, Münster, Germany.

[14]Eli and Edythe Broad Center of Regeneration Medicine and Stem Cell Research, University of California, San Francisco, USA.

[15]Department of Pediatrics, University of California, San Francisco, USA.

[16]Department of Neurology, School of Medicine, Technical University of Munich, Munich, Germany.

[17]Leibniz-Forschungsinstitut für Molekulare Pharmakologie (FMP) and Max-Delbrück-Centrum für Molekulare Medizin (MDC), Berlin, Germany.

[18]Institute of Neuropathology, University Medical Center, Göttingen, Germany.

[19]Munich Cluster for Systems Neurology, Munich, Germany.

[20]DKTK Clinical Cooperation Unit Neuroimmunology and Brain Tumor Immunology, German Cancer Research Center (DKFZ), INF 280, Heidelberg, Germany.

[21]Interdisciplinary Center for Neurosciences (IZN), Heidelberg University, Germany.

[22]Mannheim Center for Translational Neuroscience and Institute for Innate Immunoscience, Medical Faculty Mannheim, Heidelberg University, Germany.

[23]Neurocure Cluster of Excellence, Charité University Medicine Berlin

[24]Institute of Neuroanatomy, Medical Faculty Mannheim, Heidelberg University, Germany.

[25]Institute of Anatomy and Cell Biology, Johannes Kepler University Linz, Austria.

[26]Institute of Physiology I, University of Münster, Germany.

[27]Department of Ophthalmology, University of California, San Francisco, USA.

[28]Wellcome Trust-Medical Research Council Stem Cell Institute, University of Cambridge, United Kingdom.

[29]Department of Paediatrics, University of Cambridge, United Kingdom.

[30]Department of Neurosurgery, University of California, San Francisco, USA.

† Contributed equally

* Correspondence:

David H. Rowitch, MD, PhD

Department of Paediatrics, University of Cambridge

Box 116, Level 8

Cambridge, CB2 0QQ

dhr25@medschl.cam.ac.uk

+44 1223 768611

Sven Meuth, MD, PhD

Department of Neurology, University of Düsseldorf

Moorenstraße 5, 40225 Düsseldorf, Germany

meuth@uni-duesseldorf.de

+49 211 81 19532

Lucas Schirmer, MD

Department of Neurology, Medical Faculty Mannheim, Heidelberg University

Theodor-Kutzer-Ufer 1-3, 68167 Mannheim, Germany

+49 621 383 3153

lucas.schirmer@medma.uni-heidelberg.de

Declaration of Interests

RS, BH and LS filed a patent for the detection of antibodies against KIR4.1 in a subpopulation of patients with multiple sclerosis (WO2015166057A1). The other authors declare no competing interests in relation to this work.

Abstract

Multiple sclerosis (MS) is a progressive inflammatory-demyelinating disease of the central nervous system. Increasing evidence suggests that vulnerable neurons in MS exhibit fatal metabolic exhaustion over time, a phenomenon hypothesized to be caused by chronic hyperexcitability. Axonal Kv7 (outward rectifying) and oligodendroglial Kir4.1 (inward rectifying) potassium channels have important roles in regulating neuronal excitability at and around nodes of Ranvier. Here, we studied the spatial and functional relationship between neuronal Kv7 and oligodendroglial Kir4.1 channels and assessed the transcriptional and functional signatures of cortical and retinal projection neurons under physiological and inflammatory-demyelinating conditions. We found that both channels became dysregulated in MS and experimental autoimmune encephalomyelitis (EAE) with Kir4.1 channels being chronically downregulated and Kv7 channel subunits being transiently upregulated during inflammatory demyelination. Further, we observed that pharmacological Kv7 channel opening with retigabine reduced neuronal hyperexcitability in human and EAE neurons, improved clinical EAE signs and rescued neuronal pathology in oligodendrocyte-Kir4.1-deficient mice. In summary, our findings indicate that neuron-oligodendrocyte compensatory interactions promote resilience through Kv7 and Kir4.1 channels and suggest pharmacological activation of nodal Kv7 channels as a neuroprotective strategy against inflammatory demyelination.

Brief summary

Neuron-oligodendrocyte potassium shuttling promotes neuronal resilience with targeting of Kv7 channels as a neuroprotective strategy against inflammatory demyelination.

Introduction

Multiple sclerosis (MS) is the most prevalent inflammatory disease of the central nervous system (CNS) with an accumulating lesion load over time, ongoing brain atrophy and progressive neuronal injury (1). Axonal damage and eventually loss of neurons are hallmarks of pathology in progressive MS (2-4), however, little is known about the molecular mechanisms underlying chronic neuronal dysfunction caused by changes in excitability (5). For example, sustained damage to the node of Ranvier (NoR) during inflammatory demyelination results in altered ion channel distribution with direct effects on axonal conduction and neuronal excitability (6). Although changes in neuronal excitability have been described in MS animal models such as experimental autoimmune encephalomyelitis (EAE) (7) and other *in vivo* models of de- and remyelination (8-11), rational treatment strategies to normalize levels of neuronal excitability to prevent neurodegeneration are lacking.

We previously found that excitatory cortical projection neurons exhibit a high level of "transcriptional" dysregulation in MS suggestive of metabolic exhaustion and ion dysbalance (12). In particular, sodium channels exhibit a diffusely altered expression pattern along demyelinated axons (13), which contributes to changes in neuronal excitability (14, 15) and suggest ion imbalance as an interesting therapeutic target in MS (16, 17). Other studies reported that mitochondrial impairment and energy deficiency result in ion gradient breakdown and calcium overload, which further increases the risk for neuronal injury (18, 19). Hence, one intriguing, however, so far unproven hypothesis is that chronic hyperexcitablity is a key driver of neuronal vulnerability in MS (20). Reasons for enhanced neuronal excitability are likely the consequence of various factors lowering the threshold to generate action potentials in the context of chronic inflammatory demyelination.

For example, due to its role in potassium/K^+ buffering at periaxonal and paranodal spaces, oligodendroglial Kir4.1 channels, expressed at inner/outer myelin tongues and paranodes (21), are critical in stabilizing neuronal excitability and maintaining function. Independently, loss of either astroglial or oligodendroglial Kir4.1 channel function have been shown to increase neuronal excitability, triggering seizures and destabilizing axonal integrity (21-24). However, it remains unclear how oligodendroglial ion channel dysfunction mechanistically drives neuronal pathology during disease progression.

As opposed to para- and juxtanodal Kir4.1 channels, neuronal Kv7 channels are mainly responsible for outward K^+ currents and membrane repolarization at the NoR and the axon initial segment (AIS) (25, 26), regulating the threshold and frequency of action potential discharge (27). In most neurons, M-channels consist only of Kv7.2 and Kv7.3 subunits, making them the most important Kv7 subunits to regulate neuronal excitability (26, 28), which can be activated by the small molecule retigabine (RTG), (29, 30). RTG is a specific Kv7 channel opener that has shown beneficial effects in hyperexcitability-related disorders such as experimental seizure and chronic pain models (31-34), and has been studied in treatment of human epilepsy and motor neuron disease (32, 35-37). These beneficial effects of RTG are attributed to the stabilization of the neuronal resting membrane potential, thereby reducing neuronal excitability. Based on clinical trials (38-40), which demonstrated efficacy and tolerability despite side effects like skin and retina pigmentation with previous formulations, RTG was initially approved in 2011 by the FDA and the EMA for adjunctive treatment of partial-onset seizures in adult patients.

Here, we describe a functional interplay of nodal Kv7 and neighboring oligodendrocyte (OL) Kir4.1 K^+ channels in the context of K^+ shuttling, both of which we found to be

dysregulated during inflammatory demyelination. Specifically, OL-Kir4.1 channels were downregulated and Kv7 channel subunits were transiently upregulated during the course of human MS and mouse EAE, suggesting a compensatory mechanism in neurons to counteract hyperexcitability and increase resilience. We also found that early treatment with RTG assuaged neuronal degeneration and improved clinical outcomes in EAE and an OL-Kir4.1 loss-of-function model. Our findings suggest that neuron-OL K^+ shuttling at nodes of Ranvier represents a druggable interface to protect neurons against inflammatory demyelination.

Results

Ultrastructural mapping of Kv7 and Kir4.1 channels at nodes of Ranvier

We investigated the localization of neuronal Kv7 and OL-Kir4.1 channels in human and mouse optic nerve (ON) and subcortical white matter (WM) tissues (Figure 1, A-E). Kv7.2 subunits localized to nodal areas flanked by contactin-associated protein 1 (Caspr1) and in close to proximity to juxtanodal OL-Kir4.1 channels (Figure 1, A, B and D). By electron microscopy (EM), we could confirm Kv7.2 mapping to the NoR in mouse ON (Figure 1C). Notably, we observed a periodic arrangement of Kv7 (~190 nm; Figure 1A) in line with previous work (41). Further, analysis of human control and MS tissues confirmed juxta-positioning of OL-KIR4.1 and NoR-Kv7.2 channels in normal-appearing WM (NAWM) and peri-plaque WM (PPWM) lesion rim areas of ON tissues from MS patients based on MOG immunoreactivity (IR) (Figure 1B and Supplemental Table 1). By RNA *in situ* hybridization (ISH), we confirmed a high expression of *KCNJ10*, encoding KIR4.1, in both mouse and human subcortical WM OLs co-expressing *proteolipid protein 1* (*PLP*)$^+$ (Figure 1E). Of note, in cortical gray matter (GM) areas we observed a spatial relationship between *synaptotagmin* (*SYT1*)$^+$- expressing neurons and *KCNJ10*-expressing OLs (Figure 1E).

In summary, using different imaging parameters we could decipher the spatial relationship between OL-KIR4.1 and neuronal Kv7 channels across species and CNS areas, suggesting a functional crosstalk between both channels in the context of neuron-OL K^+ shuttling and homeostasis (Fig. 1F).

OL-KIR4.1 downregulation at MS lesion rims and worsened EAE in animals with ablated OL-*Kcnj10* function

To study KIR4.1 channel IR in MS ON samples, we focused on lesion rim areas and observed a reduction of OL-KIR4.1 IR at NAWM and PPWM areas (average MS

disease duration approximately 25 years) relative to controls (Figure 1G). Similarly, we detected a loss of OL-Kir4.1 IR in chronic EAE ON tissues (45 days after induction [dpi], Figure 5J). Next, we assessed axonal pathology in MS ON tissue and found a gradual loss of SMI312$^+$ axons towards the lesion center in a similar pattern as observed for OL-KIR4.1 IR (Figure 1H). To investigate consequences of ablated OL-*Kcnj10* function, we examined *Cnp-cre;Kir4.1$^{fl/fl}$* animals in the context of EAE. We noted clinical worsening and a high frequency of epileptic seizures as EAE progressed together with higher mortality rates in OL-*Kcnj10* cKO relative to controls (Supplemental Figure 1A). OL-*Kcnj10*-deficient mice showed increased numbers of Iba1$^+$ myeloid cells in spinal cord (SC) but not ON tissue samples, where we found an increase in SMI312$^+$ axon caliber size (Supplemental Figure 1, B and C).

Kv7 channel dysregulation in human MS and mouse EAE tissues

We next investigated *Kcnq2/3/5* (encoding Kv7.2/-3/-5 channel subunits) gene expression in cortical neurons. Analysis of human single-nucleus RNA-seq (snRNA-seq) (Figure 2, A and B) (12) and mouse single-cell (scRNA-seq) (42) (Supplemental Figure 4, A and B) cortical datasets revealed a strong expression of *Kcnq2/3/5* throughout all human and mouse cortical neuron populations (Figure 2, B and C; Supplemental Figure 4B) with enhanced *Kcnq3* expression in deep layer (L4-5) excitatory neurons (ENs) (Figure 2C and Figure 3A) (43-45). In MS, we found that *KCNQ3* and *KCNQ5* were downregulated in L2-6 ENs (Figure 2B, Supplemental Table 6), specifically in patients with a long disease duration (Figure 2D and Supplemental Table 7). Next, we focused on deep cortical layer neurons in MS and compared *KCNQ3* expression between control gray matter (CGM), normal-appearing gray matter (NAGM) and demyelinated gray matter (DMGM) by ISH (Figure 2, E-H). Brain tissue was analyzed for the level of demyelination by MOG IR and showed comparable levels

of microglial and astroglial reactivity (Supplemental Figure 2A and Supplemental Table 3). Notably, we observed a strong correlation between nuclear and cytoplasmic *KCNQ3* transcripts, emphasizing the validity of snRNA-seq to assess neuron-specific expression of *KCNQ2/3/5* transcripts (Figure 2F and Supplemental Figure 3, A-C). Comparing control with MS, we noted elevated *KCNQ3* transcripts in DMGM neurons compared to CGM, independent of *KCNQ3*-expressing cell numbers (Figure 2G), suggesting upregulation of *KCNQ3* in cortical deep layer neurons. Then, we found *KCNQ3* expression to be increased in MS tissues from patients with a short but decreased in those with a long disease duration (Figure 2H). No correlation was found with the extent of cortical demyelination, indicating that dysregulation of *KCNQ3* expression was independent of tissue demyelination (Supplemental Figure 3D). We next performed pseudotime-trajectory analysis and confirmed a temporal “early” upregulation of *KCNQ2/3/5* transcripts and a “late” downregulation, the latter corresponding to chronic stages of inflammation within a MS lesion (Figure 2, I-L and Supplemental Figure 3, E-G, Supplemental Table 9). Similar findings pointing towards reduced *KCNQ3* transcripts at long disease duration were observed in human retinal ganglion cells (RGCs) obtained from MS retina tissue samples (Figure 2, M and N; Supplemental Table 4; Supplemental Figure 3, H and I). Then, we focused on mouse EAE in early/inflammatory and late/chronic disease stages (Figure 3B and Supplemental Figure 2B) and assessed neuronal *Kcnq3* and Kv7.2 expression in both cortical layer 4 (L4) neurons and RGCs. By qPCR and ISH analysis, we confirmed *Kcnq3* (Figure 3, C and F) but not *Kcnq2/5* (Figure 3E) dysregulation during EAE progression in mouse cortical L4 neurons and RGCs (excitatory projection neurons of the retina) (Figure 3F), but not in non-RGC retinal nuclei (Supplemental Figure 4, C and D). In particular, cortical L4 *Kcnq3* expression gradually increased from peak of disease (14 dpi) to early-chronic EAE (30 dpi) and then decreased at late-chronic EAE

(60 dpi), although not returning to control levels (Figure 3C). We next quantified Kv7.2$^+$ nodes on protein level and found a similar trend of increased Kv7.2 expression during early/inflammatory EAE stages (Figure 3D). Notably, loss of Kv7.2$^+$ nodes in late/chronic disease stages confirmed ISH findings of decreased Kv7 expression demonstrating RNA-to-protein validation. In parallel, qPCR confirmed dysregulated *Kcnq3* expression in EAE mouse RGCs with transient upregulation in acute/early-chronic disease (Figure 3F).

To summarize, we observed both a loss of OL-KIR4.1 channels and an increase in neuronal *KCNQ3* expression under acute/early inflammatory-demyelinating conditions, possibly due to an endogenous upregulation to compensate for impaired paranodal K^+ homeostasis (Figure 3G). However, this mechanism cannot be sustained over a prolonged disease duration at both RNA and protein levels (Figure 2, D and H; Figure 3, C, D and F).

Mouse EAE is associated with neuronal hyperexcitability during peak disease

To characterize central neurophysiological effects under inflammatory-demyelinating conditions as a functional correlate of K^+ dysregulation in MS and EAE, we performed longitudinal recordings of network dynamics and neuronal single-unit activities in A1 areas (Figure 4A). Specifically, we recorded the response to two different tones before and after EAE immunization (8, 9, 46) and found enhanced neuronal response/excitability at peak of disease (14 dpi). Also, two-tone discrimination at 10 kHz was impaired in EAE (Figure 4B). Further, recordings from L4 primary auditory cortex (A1) neurons (47) confirmed increased firing (Figure 4C) with Kv7-mediated M-currents (Figure 4D) being elevated at peak of disease (12 dpi).

Kv7 regulates neuronal excitability under homeostatic and EAE conditions

To gain more insight into *Kcnq3* function under homeostatic and EAE conditions, we measured L4 neuron excitability in *Kcnq3* knockout (KO) animals. As *Kcnq3* and *Kcnq2* subunits mostly form Kv7 channel heterotetramers (48), we first excluded compensatory upregulation of *Kcnq2* in L4 neurons in *Kcnq3* KO and EAE mice by ISH (Figure 3E). By immunohistochemistry (IHC), glial cell activation (Iba1, Gfap) and axonal integrity (SMI312) were assessed, and no differences were found between *Kcnq3* KO and controls in the SC at different developmental stages (P80 vs. P180) (Supplemental Figure 5, A-C). However, there was an increase in axonal calibers in older *Kcnq3* KO animals, suggesting subtle axonal pathologies during aging, reminiscent of OL-*Kcnj10* KO (cKO) mice as described (49). In addition, shortened AIS lengths were observed in L2/3 neurons, indicating enhanced levels of neuronal excitability as reported (50) (Supplemental Figure 5D). However, loss of *Kcnq3* function had no effects during EAE (Supplemental Figure 5E). Next, we investigated electrophysiological properties and found increased firing of L4 *Kcnq3*-deficient A1 neurons under homeostatic conditions and during EAE (14 dpi) (Supplemental Figure 5, F-H). Also, EAE induction in *Kcnq3* KO mice did further augment the two-tone discrimination at 10 kHz (Supplemental Figure 5H).

Kv7 activation mitigates neuronal hyperexcitability in mouse EAE and reduces excitability in human neurons

We next explored the effects of pharmacological Kv7 channel opening to balance neuronal hyperexcitability. To assess effects on neuronal excitability and nodal M-currents, we performed whole-cell recordings (current-clamp and voltage-clamp) under homeostatic and EAE conditions. At peak of EAE (12 dpi), RTG treatment reduced the number of action potentials in A1 L4 neurons (Figure 4C). Moreover, RTG increased M-currents in line with its mode of action as an Kv7 channel activator (Figure 4D).

Additionally, increase of M-currents evoked by RTG was more prominent in neurons from EAE versus non-EAE mice supporting our previous findings of upregulated Kv7.3 expression at peak of EAE (Figure 3, C, D and F; Figure 4D). As expected, we found that *Kcnq3* deletion led to reduced M-currents with and without presence of RTG (Supplemental Figure 6A). Also, RTG treatment effects were less efficient in both non-EAE and EAE *Kcnq3*-deficient L4 neurons (Supplemental Figure 6B). To assess RTG effects on longitudinal *in vivo* network dynamics, we measured neuronal single-unit activities in A1 areas and observed that RTG-treated EAE mice (Figure 4E) showed reduced neuronal hyperactivity (Figure 4B). To clarify if RTG effects were cell-type specific and could be reproduced in humans, we tested RTG treatment in human pluripotent stem cell (PSC)-derived glutamatergic excitatory neurons (iENs) focusing on intrinsic and synaptic properties and spontaneous network activity (Figure 4, F-H). RTG application at various concentrations (0.3 µM, 1 µM, 3 µM) reduced overall iEN firing and decreased spike frequency in a dose-dependent manner, whereas blockade of (voltage-dependent) K^+ currents with 4-aminopyridine (4-AP; 100 µM) increased spontaneous firing and spike frequency (51) (Figure 4F). RTG treatment in GCaMP7s-reporter iENs (3 µM) resulted in reduced spontaneous calcium transients (Figure 4G), decreased excitatory postsynaptic current (EPSC) amplitudes and frequency but not EPSC charge (Figure 4H and Supplemental Figure 6E). 4-AP treatment, however, increased EPSC frequency (Supplemental Figure 6F). Whereas RTG (as opposed to 4-AP) did not change the resting membrane potential (Supplemental Figure 6C), it increased the threshold for action potential generation in iENs as compared to 4-AP treatment (Supplemental Figure 6D). To rule out that 4-AP treatment interferes with Kv7 channel function and Kv7-Kir4.1 K^+ shuttling, we examined evoked currents and activity of co-expressed human Kv7.2/Kv7.3 channels in *X. laevis* oocytes and found

no effect on these channels, regardless of 4-AP concentration (Supplemental Figure 6G).

RTG treatment ameliorates EAE symptoms and improves survival

We next tested *in vivo* effects of chronic RTG treatment on EAE symptoms, functional readouts and neuroglial pathology in three different treatment groups (Figure 5A). Prophylactic low-dose (1 mg/kg) RTG treatment only attenuated disease severity during chronic disease (28-30 dpi) (Figure 5B), while high-dose (10 mg/kg) prophylactic RTG treatment also ameliorated EAE progression at onset of clinical symptoms (12-14 dpi) and resulted in higher survival rates (Figure 5, C and D). Further, both prophylactic and symptomatic high-dose RTG treatment attenuated disease symptoms in chronic EAE, whereas only prophylactic high-dose RTG treatment remained significant in the mean EAE score and increased survival (Figure 5C). To assess overall axonal damage in EAE and RTG treatment effects, we measured neurofilament light chain (sNfL) serum levels (52) that correlated with EAE scores of saline (SAL) and RTG-treated EAE mice at 14 dpi and 28 dpi corresponding to peak and chronic disease (Supplemental Figure 7C). Notably, saline-treated mice showed increased EAE scores and sNfL levels as compared to RTG-treated animals. In contrast, non-specific K^+ channel blocking with 4-AP (cf. Figure 4) failed to alleviate EAE symptoms and resulted in increased mortality at 30 dpi (Figure 5D). Also, 4-AP treatment led to increased ON axon calibers, indicating subtle axon pathology (Supplemental Figure 7A), but had no effects on inflammation (Supplemental Figure 7B).

RTG treatment improves optic pathway function and limits neuroinflammation

We used the novel object recognition (NOR) test to assess recognition memory skills in EAE mice, which revealed an impairment in long-term memory (24h after habituation) upon EAE induction which was prevented by prophylactic RTG treatment starting from the day of EAE induction (Figure 5E and Supplemental Figure 7D). To investigate function of the anterior visual system in EAE, we recorded flash-light visual evoked potentials (VEP) (53, 54). Notably, only high-dose prophylactic but not symptomatic RTG treatment was effective in reducing EAE-related delays of VEP latencies and thus prevented ON dysfunction at 45 dpi (Figure 5F). Next, we examined retinal layer integrity during EAE by optical coherence tomography (OCT). We observed EAE-related thinning of inner retinal layers reflecting retinal neurodegeneration (55), which was ameliorated by prophylactic RTG treatment. Prophylactic RTG treatment demonstrated protective effects against EAE-related neuronal loss in the visual system by preserving RGC and SMI312^{+} axon density in ON tissue 45 dpi (Figure 5, G and H). Also, prophylactic RTG treatment resulted in ameliorated inflammatory activity relative to SAL treatment (Figure 5I). Consistent with findings in MS ON (Figure 1G), OL-Kir4.1 channel expression was decreased in EAE ON compared to non-EAE controls; however, prophylactic RTG treatment preserved OL-Kir4.1 expression levels at pre-immunization baseline levels (Figure 5J). To rule out immune-related effects of RTG treatment, we profiled brain-infiltrating immune cells and observed no differences between saline and RTG-treated animals (Supplemental Figure 7E).

In conclusion, prophylactic RTG treatment was well tolerated, improved functional and structural EAE outcome and delayed neuronal loss in the absence of an anti-inflammatory effect (Figure 5K).

Chronic RTG treatment is beneficial in mice with OL-*Kcnj10* loss of function

We previously showed that loss of OL-*Kcnj10* function results in progressive neurodegeneration, thus resembling aspects of chronic EAE and progressive MS (49). To investigate whether pharmacological Kv7 opening might also be beneficial when para- and juxtanodal K^+ siphoning through OL cells is impaired, we tested OL-*Kcnj10* KO mice and control littermates with high-dose RTG (10 mg/kg daily) compared to saline over 5 months starting at P40 until 6 months of age corresponding to P180 (Figure 6A). Chronic RTG treatment improved VEP latencies at P80, but not at later timepoints; likewise, RTG treatment could assuage but not prevent age-related IRL thinning (Figure 6B). Nevertheless, RTG resulted in increased survival in OL-*Kcnj10* KO mice (Figure 6B). At structural level, RTG protected RGCs from degeneration in OL-*Kcnj10* KO mice and showed protective effects on $SMI312^+$ axon survival and $CASPR^+$ paranodes (Figure 6C and Supplemental Figure 8, A and B). RTG treatment also protected against an accumulation of dystrophic $SMI32^+$ axons and an increase in axon caliber at P180 in OL-*Kcnj10* KO mice (Figure 6D and Supplemental Figure 8A). Further, we noted a mild reduction of inflammation but no effects on astrogliosis in RTG-treated OL-*Kcnj10* KO ONs at P180 (Supplemental Figure 8C).

Discussion

We describe a “nodal-glial” interface that appears necessary for long-term neuron-OL K^+ shuttling and homeostasis during inflammatory demyelination and demonstrate the importance for nodal-glial interaction during health and disease, similar to previous work on neuron-microglia crosstalk (56). This spatial and functional interface comprises outward rectifying Kv7 (41) and inward-rectifying OL-Kir4.1 K^+ channels at the NoR and the AIS (49). During repolarization Kv7 channels shuttle K^+ ions from the axolemma into paranodal spaces, where K^+ is “siphoned” to areas of low K^+ concentration by astroglial and OL-Kir4.1 channels. While both neuronal and OL channels were dysregulated in human MS and mouse EAE, OL-Kir4.1 channels became chronically downregulated in WM MS and EAE tissues. In contrast, Kv7 channel subunits (in particular Kv7.3) appeared to be transiently upregulated during early inflammatory periods and downregulated in chronic disease.

Our findings of Kv7 channel upregulation in acute disease stages are consistent with other work on altered expression and redistribution of sodium channels along demyelinated axons in MS and related models (57, 58), resulting in conduction defects, breakdown of ion gradients and axonal degeneration (6, 59). Moreover, shortened internodal length and an increase of nodal density with concomitant increase in sodium channels are associated with enhanced axonal/neuronal excitability (59, 60), thus providing an explanation for increased Kv7 expression not only due to an increased nodal density but also as an adaptive response to hyperexcitability.

Might early and transient upregulation of Kv7 subunits represent an endogenous compensatory mechanism that counteracts enhanced neuronal excitability in MS and EAE? If so, our data demonstrates that this mechanism ultimately fails during

progressive disease characterized by a combined loss of Kir4.1 and Kv7 channel function. Specifically, we found that impaired Kv7 function was driven by dysregulated *Kcnq3* (but not *Kcnq2*) gene expression during EAE. We further demonstrated that chronic *Kcnq3* loss-of-function increases neuronal excitability *ex vivo* and *in vivo* pointing towards a key role of this subunit for network function under physiological and disease conditions. However, whereas lost *Kcnq3* function did not worsen EAE, we found that a chronic loss of OL-*Kcnj10* function worsened symptoms and increased mortality in EAE. Such loss-of-function studies provide therefore evidence that Kv7 and Kir4.1 channels function in a synergistic way to establish and maintain saltatory conduction over time. Eventually, this synergistic interplay collapses under chronic inflammatory-demyelinating conditions as in progressive MS and EAE.

Finally, we tested whether it was possible to stabilize K^+ homeostasis and prevent neuronal hyperexcitability during EAE using small molecules that could potentially translate to the clinic. To activate outward rectifying currents at the NoR, we treated EAE mice with RTG, a specific Kv7 channel opener. By *ex vivo* recordings, we validated that RTG treatment fostered axonal K^+ outflow and reduced the firing rate of neurons in both control and EAE brain tissues. Under *in vivo* conditions, we found that RTG treatment starting at EAE induction improved neurological and cognitive symptoms and prevented neurodegeneration in EAE and during early adulthood in cKO animals lacking OL-Kir4.1 channels. We demonstrated that these effects were consistent between various functional circuits comprising the visual, the auditory and the motor system. Also, RTG treatment mitigated the loss of OL-Kir4.1 channel expression in EAE likely due to an overall improved tissue preservation and increased axonal K^+ outflux stimulating OL-mediated siphoning of K^+ ions. Collectively, our data suggest that “early” neuroprotection though Kv7 channel opening might represent an

interesting approach to delay clinical progression and “late” neurodegeneration by stabilizing neuron-OL K^+ shuttling over a prolonged period.

As opposed to RTG, clinical symptoms were not altered and mortality was increased in EAE mice treated with 4-AP, a fairly unspecific Kv channel blocker with no obvious effects on Kv7 channel function as demonstrated. Of note, our data refute previous results when EAE animals were treated with 4-AP via drinking water versus daily intraperitoneal injections in our study (61), which makes a direct comparison difficult due to the different routes of administration. The increase in mortality was most likely the consequence of neuronal hyperexcitability and development of epileptic seizures, which was regularly seen in EAE animals treated with 4-AP. These opposing effects could be validated *in vitro* when recording from human iEN cells treated with either RTG or 4-AP. Here, we found that RTG but not 4-AP could reduce neuronal firing, increased the threshold for action potential generation and, moreover, was able to stabilize neuronal network activity. Notably, we cannot completely rule out anti-inflammatory effects of RTG treatment, although our data rather suggest a primarily role in regulating neuronal excitability with potentially secondary anti-inflammatory effects due to improved neuronal preservation.

Previously, the most common adverse effects of RTG treatment in humans were dose-related and included somnolence and dizziness, while long-term therapy was associated with skin and retina discoloration. Rare but potentially serious adverse effects of previous formulations included urinary retention and a reduction in visual acuity due to retinal pigmentation. Hence, new drug formulations targeting Kv7 channels need to be evaluated, particulary, in the context of visual impairment during long term treatment (38-40, 62, 63).

In summary, our findings highlight novel neuron-OL compensatory mechanisms in chronic inflammatory demyelination and suggest a rational neuroprotective approach through modulation of K^+ levels. Treatment with RTG provided proof of concept for this notion, showing how endogenous Kv7 might be recruited to counteract neuronal hyperexcitability in progressive MS and related neuroimmune diseases. Thus, pharmacological Kv7 channel activation represents a promising therapeutic strategy to counteract progressive neurodegeneration in MS and beyond.

Material and Methods

Transgenic mouse lines

Kcnj10 conditional KO mouse strains were maintained at the University of California, San Francisco (UCSF) in a specific pathogen-free animal facility. Conditional knockouts were obtained by crossing *Kir4.1*$^{fl/fl}$ mice with *Cnp-cre* mice. *Cnp-cre* transgenic mice were obtained from Klaus-Armin Nave (Max Planck Institute of Experimental Medicine, Göttingen), and had been previously generated (64). *Kir4.1*$^{fl/fl}$ mice were obtained from Ken D. McCarthy (Chapel Hill, NC, USA) and had been generated as previously described (22, 65). *Olig2-tva-cre* transgenic mice were generated as previously described (66). Long-term treatment experiments (Figure 6 and Supplemental Figure 8) were performed with *Olig2-cre;Kir4.1*$^{fl/fl}$ versus cre-negative *Kir4.1*$^{fl/fl}$ mice. *Kcnq3* KO mouse strains were maintained at the animal facility of University Hospital Münster under pathogen-free conditions. *Kcnq3*$^{-/-}$ mouse strains were obtained from Thomas Jentsch, Leibniz-Forschungsinstitut für Molekulare Pharmakologie (FMP) and Max-Delbrück-Centrum für Molekulare Medizin (MDC), Berlin and have been previously described (67, 68). All mice were kept on a C57BL/6J background. *Kir4.1*$^{fl/fl}$ littermates and wild-type mice were used as controls.

Mouse tissue processing

Mice were transcardially perfused with PBS or 4% paraformaldehyde (PFA) for IHC and 4% formaldehyde and 0.2% glutaraldehyde in 0.1 M PBS containing 0.5% NaCl for immunolabeling. For IHC, cryosections of mouse and human (snap-frozen) tissues were collected using a CM3050S cryostat (Leica Microsystems). For electron microscopy, tissue was post-fixed for 24h, embedded in 10% gelatin, and infiltrated overnight with 2.3 M sucrose in 0.1 M PBS. Ultrathin cryosections of embedded tissue

511 in gelatin blocks were made using a UC7 cryo-ultramicrotome (Leica) and a 35° cryo-
512 immuno-diamond knife (Diatome).
513
514 **Conventional immunohistochemistry**
515 Sections were fixed in ice-cold methanol or 4% PFA and blocked in PBS-T and10%
516 goat serum (1% BSA, 0.2% fish skin gelatin, 0.1% Triton in 0.1 M PBS for for βIV-
517 spectrin staining) for 30 min (at least 60 min for βIV-spectrin staining). Primary antibody
518 incubations were carried out overnight at 4°C; slides were incubated with secondary
519 antibodies for 2h. For chromogenic assays, sections were incubated with biotinylated
520 secondary IgG antibodies (Thermo Fisher, 1:500) followed by avidin-biotin complex for
521 1h incubation (Vector, 1:500) and subsequent color revelation using diaminobenzidine
522 (Dako). Hematoxylin and eosin staining was carried out for diagnostic purposes. Slides
523 with fluorescent antibodies were mounted with DAPI-Fluoromount-G (Thermo Fisher).
524
525 **Primary antibodies**
526 Antibodies for IHC and western blots: mouse anti-CASPR (75-001, NeuroMab, 1:250);
527 rabbit anti-CASPR (ab34151, Abcam, 1:1,000); rabbit anti-Kv7.2 (ab22897, Abcam,
528 1:250); rabbit anti-Kv7.2 (368103, Synaptic Systems, 1:300-1,000); guinea pig anti-
529 Kv7.2 (raised against peptide VQKSRNGGVYPGTSGEKKL, coupled by a C-terminally
530 added cysteine to Keyhole Limpet Hemocyanin; named Q2Agp1 (67), provided by T.
531 Jentsch, FMP and MDC, Berlin; 1:500); rat anti-human KIR4.1 (clone 20F9 generated
532 against an extracellular domain of human KIR4.1 [peptide sequence
533 AHGDLLELDPPANHT], 1:1,000); rabbit anti-KIR4.1 (APC-165, Alomone Labs,
534 1:1,000); rabbit anti-KIR4.1 (APC-035, Alomone Labs, 1:3,000); mouse anti-NOGO-A
535 (clone 11C7, gift from Martin Schwab, University of Zurich, Switzerland; 1:3,000);
536 mouse anti-MOG (clone 8-18C5, Millipore Sigma, 1:1,000 [1:200 after ISH]); rat anti-

MBP (MAB386, clone 12, Merck, 1:200); rabbit anti-Iba1 (019-19741, Wako, 1:500); mouse anti-SMI312 (clone SMI312, 837904, BioLegend, 1:1,000); anti-GFAP (13-0300, Thermo Fisher, 1:200); rabbit anti-βIV-spectrin (provided by Maren Engelhardt, University of Linz, Austria, 1:1,000 (50); chicken anti-NeuN (ab134014, Abcam, 1:1,000); goat anti-Brn3a (sc-31984, Santa Cruz Biotechnology, 1:200); mouse anti-Neurofilament H (NF-H); nonphosphorylated (clone SMI32, 801701, BioLegend, 1:10,000); anti-APC (clone CC1, OP80, Millipore Sigma, 1:500). For all experiments, negative control sections without primary antibodies were processed in parallel. All IHC analysis was carried out blinded.

In situ RNA hybridization

Chromogenic single-molecule and multiplex ISH was performed according to published protocols (12, 69) and manufacturer's recommendations (RNAscope 2.5 HD Reagent Kit-RED; RNAscope multiplex fluorescent v2 assay kit, ACD Biotechne). Manual RNAscope assay probes: *KCNQ3* (human, chromogenic single ISH); *KCNJ10*, *SYT1*, *PLP1* (human, multiplex ISH); *Kcnq3*, *Kcnq2*, *Syt1*, *Rorb, Plp1, Kcnj10* (mouse, multiplex ISH). For multiplex ISH, probes were labeled with TSA Plus Fluorophores (Fluorescein, Cyanine3, Cyanine5, Akoya Biosciences) and nuclei were labeled with DAPI. Following red chromogenic single-molecule ISH, IHC and hematoxylin staining of nuclei were performed. As quality control, negative (DapB) and positive ISH probes (*PPIB*, *Polr2a*, *Ppib* and *Ubc*) were run in parallel.

Quantification of _in situ_ RNA transcripts

The number of individual RNA signals was quantified using the automated particle analysis plug-in of ImageJ Fiji software (v2.1). For human *KCNQ3* quantification, 11 MS samples were screened for demyelination using MOG IHC. 7 NAGM and 20

DMGM upper cortical layer (L1-3) and 20 NAGM and 14 DMGM deep cortical layer areas (L4-6) were selected. For 6 control samples, 19 upper layer and 18 deep layer areas were selected. 3-4 ROIs were quantified for each area and mean value per condition and layer was assessed to determine the average *KCNQ3* expression per sample.

Human and mouse snRNA-seq data acquisition for bioinformatic analyses

Expression matrices and associated metadata were obtained from UCSC Cell Browser (https://cells.ucsc.edu/?ds=ms) for Schirmer et al (2019) dataset (12) (PRJNA726991) and Gene Expression Omnibus (GEO) database for Tasic et al. (2018) (42) (GSE115746). For analysis of Schirmer et al dataset (12) the expression matrix was normalized using Seurat (v3.2.3) SCTransformation (70) with default parameters. Principal component analysis (PCA) was done using Seurat RunPCA() calculating top 50 principal components (PCs). 15 PCs were taken as input for Seurat RunUMAP(), FindNeighbors() and FindClusters(). Finally, subset of neurons and samples originating from the London brain bank (Supplemental Table 5) were renormalized using the same procedure and including 14 PCs for clustering. Tasic et al. dataset (42) was reanalyzed in the same way. Since barcode annotation discrepancies were found between matrix and metadata provided by authors, only barcodes present in both matrix and metadata were included (Supplemental Table 10).

Trajectory inference analysis

A trajectory for human excitatory cortical L2/3 neurons was inferred using the Monocle package v.3 beta (71). Briefly, transcriptomes of all L2/3 nuclei were dimensionally reduced by computing 50 PCs; batch effects were removed using batchelor algorithm (72), where each sample was treated as batch. Next, unsupervised trajectory was

589 inferred through the reduced space. The resulting tree was ordered with the tree root
590 located where most nuclei of control samples clustered. Finally, branches were
591 analyzed separately by dividing branches between starting point (root) and ending
592 point (furthest point of the pseudotime trajectory).
593
594 **Human induced pluripotent stem cell derived neurons**
595 Induced excitatory forebrain neurons (iENs) were differentiated from induced
596 pluripotent stem cells (iPSCs) derived from a healthy donor (HD6, Heidelberg
597 University), according to a protocol developed by Zhang et al. (73). iPSCs were
598 infected with lentiviruses expressing rtTA (Ubiquitin promoter) and Neurogenin-2
599 (NGN2) (73) and puromycin (rtTA promoter). After 1 day, doxycycline was used to
600 trigger NGN2 and Puromycin expression, followed by puromycin selection for 2 days.
601 For calcium imaging, cell were additionally infected with a lentivirus expressing
602 GCaMP7s (Ubiquitin promoter). All measurements were performed 4-5 weeks after
603 derivation. Coverslips containing iENs were placed in a recording chamber under a
604 Olympus BX51WI microscope equipped with DIC and fluorescence capabilities.
605 Recordings were performed at 24 ± 1°C. In all experiments, 4-AP (Sigma; 100 µM) and
606 RTG (Alomone; 0.3 µM, 1 µM, 3 µM) were bath-applied. A CMOS camera (Thorlabs)
607 was used to image in green channel (100 ms pulses, LED 488 nm) every 2 seconds.
608 In patch clamp experiments, cells were approached and patched under DIC with 3 MΩ
609 pipettes using a Narishige PC-10 puller (Japan). Neurons were maintained at -70 mV
610 holding potentials using an Axoclamp 700B amplifier controlled by Clampex11
611 software (Molecular Devices). Series resistance varied between 8-10 MΩ. iENs in the
612 recording chamber were continuously perfused with oxygenated (95% O_2 / 5% CO_2)
613 bath solution containing (in mM): 125 NaCl, 2.5 KCl, 1 $MgCl_2$, 2 $CaCl_2$, 25 glucose,
614 1.25 NaH_2PO_4, 0.4 ascorbic acid, 3 myoinositol, 2 Na-pyruvate, and 25 $NaHCO_3$ pH

7.4 and 315 mOsm. Synaptic currents were recorded with an internal solution that contained (in mM): 140 Cs-Methanesulfonate, 0.5 EGTA, 1 $MgCl_2$, 10 HEPES, 2 ATP-Magnesium, 0.4 GTP-Sodium, 10 Na-PhosphoCreatine, pH 7.2, 310 mOsmoles. Intrinsic and AP properties were recorded using a pipette solution containing (in mM): 125 $KMeSO_3$, 20 KCl, 2 $MgCl_2$, 0.5 EGTA, 4 MgATP, 0.3 NaGTP, 10 Na-Phosphocreatin, and 10 HEPES-KOH (pH adjusted to 7.3, 315 mOsm). Current-clamping membrane potentials were kept around -70 mV using small (less than 30 pA) holding currents, and step currents were injected to elicit APs. Analysis and plotting of imaging data was performed using FluoroSNNAP (https://www.seas.upenn.edu/~molneuro/FluoroSNNAP/user_guide.pdf) and custom R macros (https://github.com/AcunaLabUHD/Physiology-Macros/blob/main/calcium%20summaries.v1.1.R). Spikes and synaptic current properties were analyzed using custom macros written in IgorPro 6.11 (Wavemetrics) (https://github.com/AcunaLabUHD/Physiology-Macros/blob/main/synaptic%20transmission_v4.3.ipf) or Clampfit11 software (Molecular Devices). Data derived from different batches were normalized by the control condition.

Tissue preparation for electrophysiological experiments

Naive and MOG_{35-55}-immunized C57BL/6J and *Kcnq3* KO female mice (8-12 weeks) were anesthetized and decapitated. Brains were removed and dissected in ice-cold slicing solution containing (in mM): KCl, 2.5; NaH_2PO_4, 1.25; $MgSO_4$, 10; PIPES, 20; Glucose, 10; Saccharose, 200; $CaCl_2$, 0.5; pH 7.35. Acute coronal brain slices containing the primary auditory cortex (A1) were prepared on a vibratome (Leica) and hereafter incubated for 30 min in a warm (32ºC) carbogenated solution containing (in

mM): NaCl, 1.25; $NaHCO_3$, 240; NaH_2PO_4, 12.5; KCl 25; Glucose 10; $CaCl_2$, 2; $MgSO_4$, 2; pH 7.35.

Whole-cell patch clamp recordings

Following an incubation period of 30 min at RT, slices were transferred to a recording chamber constantly perfused at a flow rate of ~2 ml/min with carbogenated artificial cerebrospinal fluid containing (in mM): NaCl, 120; KCl, 2.5; NaH_2PO_4, 1.25; $NaHCO_3$, 22; Glucose, 25; $CaCl_2$, 2; $MgSO_4$, 2; pH 7.35. Whole-cell recordings were performed on the soma of L4 A1 pyramidal neurons using glass patch pipettes filled with a K^+ gluconate-based intracellular solution containing (in mM): NaCl, 10; K-gluconate, 88; K_3-citrate, 20; HEPES, 10; BAPTA, 3; Phosphocreatine, 15; $MgCl_2$, 1; $CaCl_2$, 0.5; Mg-ATP, 3; Na-GTP, 0.5; pH 7.25; 295 mOsmol/kg. Typical electrode resistance was 5-6 MΩ. Series resistance was within 5-15 MΩ and a compensation of ≥40% was routinely applied. Patch pipettes were connected to an EPC-10 amplifier (HEKA Elektronik) to measure electrical activity. Recordings were governed by Patchmaster software (HEKA Elektronik) and corrected for the liquid junction potential.

Current-clamp analysis

Current-clamp experiments were performed in a bath solution without blockers (see above). Resting membrane potential was adjusted to -60 mV by DC current injection and the degree of single cell excitability was characterized in response to a depolarizing current injection of 100 pA (1.5 s). Number of action potentials was assessed under control conditions and following application of RTG (30 µM) to the bath solution. FitMaster (HEKA Elektronik) and PEAK Software were used for the analysis (Meuth IT Consulting).

Voltage-clamp recordings

Variations in current amplitude were measured in a bath solution (see above) containing (in μM): mibefradil, 2; nifedipine, 1; ZD7288, 30; tetrodotoxin, 0.5. Membrane outward currents were elicited at a holding potential of -65 mV, followed by a depolarizing step to -45 mV. Thereafter, neurons were repolarized to -60 mV. The duration of each pulse was 4 s. Current amplitudes were analyzed at the furthermost 500 ms of the depolarizing voltage step of -45 mV under control conditions and following RTG application (30 μM), using the software FitMaster (HEKA Elektronik).

Stereotactic surgeries

For craniotomy surgery and electrode implantation, anesthesia was induced and maintained (8). Animals were anaesthetized and positioned in a stereotactic frame (ASI Instruments). The skin was incised, the skull was disinfected and leveled, and a craniotomy was performed (A1, antero-posterior, -2.18 mm; lateral, +4.2 mm from bregma; dorso-ventral, 1 mm from brain surface). Microwire arrays housing eight electrodes (Stablohm 650, California Fine Wire) were implanted unilaterally (left hemisphere) into cortical L4 of A1 and fixed with dental cement (Pulpdent-GlassLute). A ground electrode was placed in proximity of the midline over the cerebellar region (antero-posterior, -5.8; lateral, +0.5 mm from bregma, right hemisphere). Gold-plated wire tips with a cathodal current of 1 μA were submerged in a gold solution to reduce the impedance to 150-300 kΩ. The animals' health status and recovery were assessed daily for 10 days after the procedure.

***In vivo* electrophysiological recordings**

After 10 days of recovery following surgery, C57BL/6J and *Kcnq3* KO mice were MOG_{35-55} immunized and recordings of unit activity were performed at 12 and 14 dpi.

Recordings obtained prior to EAE induction served as control. Recordings were performed in freely moving mice before and during the presentation of an auditory stimulus consisting of 6 repetitive low- or high-frequency tones (2.5 kHz/10 kHz at 85 dB). Extracellular unit activities were recorded using a Multichannel Amplifier System (Alpha Omega) and stored on a personal computer. Signals were band-pass filtered at 100 Hz to 20 kHz and processed at a sampling-rate of 40 kHz. Individual neuronal spikes were sorted by time-amplitude window discrimination and PC analysis (Offline Sorter, Plexon) and validated through quantification of cluster separation (9).

Single-unit analysis

Firing rates and z-scores of sorted neurons were analyzed relative to baseline activity in 1s segments (1 bin), 60s before and during the presentation of an auditory stimulus, with a custom MATLAB interface (MathWorks). Firing rates of individual units were z-scored to their mean baseline activity. Neurons were considered responsive if ≥1 bin showed z-score ≥1.96 (p=0.05) in response to stimulus presentation (9, 46).

EAE induction and clinical scoring

EAE was induced in female C57BL/6J mice (Jackson Lab) at 8-14 weeks of age as previously described (74). Mice were immunized subcutaneously with MOG_{35-55} peptide (100µg, Anaspec, UCSF; 200µg, Peptides & Elephants, UKE; 200µg, Charité, UKM) in complete Freund's adjuvant (CFA) containing non-viable mycobacterium tuberculosis (1 mg/ml, UKE; 2 mg/ml, UCSF; 5 mg/ml, UKM; Difco). In addition, pertussis toxin (200 ng, List Biological Laboratories, UCSF; 300 ng, Calbiochem, UKE; 400 ng, Enzo Life Sciences, UKM) was injected i.p. on day of immunization (0 dpi) and 48 h later (2 dpi). Mice were scored daily: 0: no clinical signs; 0.5: distal limp tail; 1: limp tail; 1.5: inability to turn immediately when flipped on the back; 2: weakness of

hind limb; 2.5: severe hind limb paresis; 3: severe bilateral hind limb paresis with paralysis of one hind limb; 3.5: complete bilateral hind limb paralysis; 4: beginning forelimb paresis; 4.5: severe forelimb paresis; 5: moribund. Animals reaching a clinical score of either ≥ 3.5 for more than 4 (UKM) or 7 (UKE) consecutive days or a clinical score of ≥ 4 (UKM, UKE, UCSF) were taken out from experimentation and were euthanized. The last score observed was included for the analysis until the last experimental time point. Cumulative clinical scores were determined as the mean scores of each mouse from the day of clinical onset and for total time of the experiments, divided by the number of days of sickness.

RTG and 4-AP treatment in EAE mice

Mice from treatment groups received either RTG, 4-AP or SAL as i.p. injections. RTG (1 mg/kg or 10 mg/kg body weight) and 4-AP (250 µg/kg) were given as a sterile solution dissolved in SAL, as described in other reports (75). To distinguish presymptomatic and symptomatic treatment, EAE mice were treated daily starting at 0 dpi with either SAL, RTG or SAL with change to RTG after achieving an EAE score ≥ 0.5 (1 mg/kg BW) or ≥ 2 (10 mg/kg BW). For chronic RTG treatment of transgenic mouse lines, RTG (10 mg/kg) was applied between P40 and P180 according to previous reports (76-78). Control mice were injected i.p. daily with the same volume of 0.9% SAL.

Data and material availability

All data are available in the main text and supplemental materials. Human snRNA-seq data were obtained from the UCSC Cell Browser (https://cells.ucsc.edu/?ds=ms) under accession number PRJNA726991. Mouse snRNA-seq data were obtained from GEO database under accession number GSE115746.

744

745 **Statistics**

746 All results are presented as mean ± SEM. Statistical analysis was performed using
747 parametric (unpaired t-test comparing two groups; one-way and two-way ANOVA test
748 comparing three or more groups) or non-parametric (Kruskal Wallis test comparing
749 three groups) tests. Tests were performed using 2-tailed analysis unless stated
750 otherwise. The significance cut-off was set at $p<0.05$. P values were designated as
751 follows: *$p<0.05$, **$p<0.01$, ***$p<0.001$, ****$p<0.0001$. Statistical analyses were
752 performed using GraphPad Prism software version 9.0.

753

754 **Study approval**

755 Human postportem tissue samples were obtained from the UK MS Society Tissue
756 Bank (London), the Netherlands Brain Bank (Amsterdam) and Johns Hopkins
757 University Medical School, Baltimore (Maryland, USA) following fully informed consent
758 by tissue donors according to national ethical guidelines and legal regulations. In
759 particular, ethical approval was obtained from the UK National Research Ethics
760 Committee (08/MRE09/31) and the Independent Review Board of the Vrije Universiteit
761 Medical Center Amsterdam (IRB00002991, 2009/148). Control tissue samples were
762 obtained from individuals without neuropathological findings. In total, postmortem brain
763 tissue blocks from 10 MS patients and 6 controls, ON tissues from 9 MS and 4 control
764 subjects and eyeball/retina from 7 MS patients and 6 controls were used. Supplemental
765 Tables 1-4 summarize human tissue samples. Animal experiments were performed at
766 animal facilities of University Hospital Münster (UKM), University Medical Center
767 Hamburg-Eppendorf (UKE) and University of California, San Francisco (UCSF) in
768 accordance to the national ethical guidelines and legal regulations (Landesamt für
769 Natur, Umwelt und Verbraucherschutz Nordrhein-Westfalen, approval ID 81-

02.04.2018.A266/84-02.04.2015.A585 [UKM]; Behörde für Soziales, Familie, Gesundheit und Verbraucherschutz Hamburg ,G122/17 [UKE]; Institutional Animal Care and Use Committee and Laboratory Animal Resource Center San Francisco, AN110094 [UCSF]). All mice were maintained on a 12 hours light/dark cycle with food and water available *ad libitum*.

Authors contribution

HK, LF, JD, DHR, SGM and LS designed the experiments. HK, LF, JD, SS, ACH, JC, CM, ED, WM, CC, AKP, MG, AZ, VNN, AD, MC, TM, CLM, JKS, JHS, PD, NR, KS, MC, RS and LS performed the experiments. HK, LF, JD, SS, CM, AZ, PD and LS analyzed the data. HK and LS wrote the manuscript. CS, BH, GS, MP, TJ, ME, TB, KAN, PAC, MAF, AJG, CA, DHR, SGM and LS participated in data analysis and discussion of results. HK and LS completed the final review and submitted the manuscript. All authors contributed to the article and approved the submitted version. The order of the co–first authors was determined on the basis of their efforts and contributions to the study.

Acknowledgments

We thank the UK MS Society Tissue Bank and the Netherlands Brain Bank for providing human postmortem retina, ON and cortex tissue samples from MS and control donors. We thank Dr. Heidrun Potschka (Munich University), Dr. Holger Lerche and Dr. Stephan Lauxmann (both Tübingen University) for advice and comments on the study. We thank Matthew Smith (Johns Hopkins University) for technical assistance.

Funding

This work was supported by the Swiss National Science Foundation (Eccellenza Professorship to AKP), the Propatient Foundation, the Goldschmidt-Jacobson Foundation, intramural funding from the University of Basel (all to AKP), the Medical Faculty Mannheim of Heidelberg University (to LS, ME), research grants from the Hertie Foundation (medMS MyLab, P1180016 to LS, medMS fellowship to HK), the UCSF Program for Breakthrough Biomedical Research (to ACH), the Adelson Medical Research Foundation (to DHR, KAN), the Cambridge Biomedical Research Center (to DHR), grants from the National Institute of Neurological Disorders and Stroke (NS040511, to DHR) and the Wellcome Trust (to DHR), the European Research Council (ERC AdG “AxoGLIA” and “MyeliNANO”, to KAN; ERC AdG “Myel-IN-Crisis”, to DHR ERC StG “DecOmPress”, to LS), the National Multiple Sclerosis Society (FG-20102-A-1, to ACH; FG-1708-28871, to AKP; FG-1902-33617 and RFA-2203-39300, to LS), the Italian Multiple Sclerosis Society (2013/B/4, to CC), Fonds de recherche du Québec – Santé (270746 to MG), the German Multiple Sclerosis Society (V6.2, to MAF), the Leibniz Society (SAW grant to TJJ), the German Research Foundation through DFG collaborative research projects (TRR43 to KAN; TRR273 to CS, CRC-TR128 to TB and SGM; FOR2289 to MAF; SFB1158 to CA; FOR2690 and GRK2727,

811 to LS), individual research grants (BU1019/16-1 to TB; FR1720/11-2 to MAF;
812 EN1240/2-1 to ME; STA1389/5-1 to CS; SCHI1330/4-1 to LS), a Heisenberg
813 Fellowship (SCHI1330/6-1, to LS), Chica and Heinz Schaller Foundation, the Fritz
814 Thyssen Foundation (10.21.0.019MN, to CA), the Brain & Behavior Research
815 Foundation (NARSAD, Young Investigator award 2019, to CA), Clinician-Scientist
816 Fellowship from the Stifterverband and the Werner Otto-Stiftung (07/100, to CM), the
817 DAAD/ANID fellowship (57451854/62180003, to JC) and the DFG under Germany's
818 Excellence Strategy (EXC171 to KAN; EXC2067 to CS and WM; EXC2145 to BH;
819 EXC257 to TJJ).

References

1. Reich DS, Lucchinetti CF, and Calabresi PA. Multiple Sclerosis. *New England Journal of Medicine.* 2018;378(2):169-80.
2. Friese MA, Schattling B, and Fugger L. Mechanisms of neurodegeneration and axonal dysfunction in multiple sclerosis. *Nat Rev Neurol.* 2014;10(4):225-38.
3. Schirmer L, Antel JP, Brück W, and Stadelmann C. Axonal loss and neurofilament phosphorylation changes accompany lesion development and clinical progression in multiple sclerosis. *Brain pathology (Zurich, Switzerland).* 2011;21(4):428-40.
4. Peterson JW, Bo L, Mork S, Chang A, and Trapp BD. Transected neurites, apoptotic neurons, and reduced inflammation in cortical multiple sclerosis lesions. *Annals of neurology.* 2001;50(3):389-400.
5. Caramia MD, Palmieri MG, Desiato MT, Boffa L, Galizia P, Rossini PM, et al. Brain excitability changes in the relapsing and remitting phases of multiple sclerosis: a study with transcranial magnetic stimulation. *Clin Neurophysiol.* 2004;115(4):956-65.
6. Lubetzki C, Sol-Foulon N, and Desmazieres A. Nodes of Ranvier during development and repair in the CNS. *Nat Rev Neurol.* 2020;16(8):426-39.
7. Ellwardt E, Pramanik G, Luchtman D, Novkovic T, Jubal ER, Vogt J, et al. Maladaptive cortical hyperactivity upon recovery from experimental autoimmune encephalomyelitis. *Nat Neurosci.* 2018;21(10):1392-403.
8. Cerina M, Narayanan V, Gobel K, Bittner S, Ruck T, Meuth P, et al. The quality of cortical network function recovery depends on localization and degree of axonal demyelination. *Brain Behav Immun.* 2017;59:103-17.

9. Narayanan V, Cerina M, Göbel K, Meuth P, Herrmann AM, Fernandez-Orth J, et al. Impairment of frequency-specific responses associated with altered electrical activity patterns in auditory thalamus following focal and general demyelination. *Exp Neurol.* 2018;309:54-66.
10. Hamada MS, and Kole MH. Myelin loss and axonal ion channel adaptations associated with gray matter neuronal hyperexcitability. *J Neurosci.* 2015;35(18):7272-86.
11. Hamada MS, Popovic MA, and Kole MH. Loss of Saltation and Presynaptic Action Potential Failure in Demyelinated Axons. *Front Cell Neurosci.* 2017;11:45.
12. Schirmer L, Velmeshev D, Holmqvist S, Kaufmann M, Werneburg S, Jung D, et al. Neuronal vulnerability and multilineage diversity in multiple sclerosis. *Nature.* 2019;573(7772):75-82.
13. Craner MJ, Newcombe J, Black JA, Hartle C, Cuzner ML, and Waxman SG. Molecular changes in neurons in multiple sclerosis: altered axonal expression of Nav1.2 and Nav1.6 sodium channels and Na+/Ca2+ exchanger. *Proc Natl Acad Sci U S A.* 2004;101(21):8168-73.
14. Smith KJ. Sodium Channels and Multiple Sclerosis: Roles in Symptom Production, Damage and Therapy. *Brain Pathology.* 2007;17(2):230-42.
15. Waxman SG. Axonal conduction and injury in multiple sclerosis: the role of sodium channels. *Nature Reviews Neuroscience.* 2006;7(12):932-41.
16. Morsali D, Bechtold D, Lee W, Chauhdry S, Palchaudhuri U, Hassoon P, et al. Safinamide and flecainide protect axons and reduce microglial activation in models of multiple sclerosis. *Brain.* 2013;136(4):1067-82.

869 17. Black JA, Liu S, Carrithers M, Carrithers LM, and Waxman SG. Exacerbation
870 of experimental autoimmune encephalomyelitis after withdrawal of phenytoin
871 and carbamazepine. *Ann Neurol.* 2007;62(1):21-33.
872 18. Mahad D, Ziabreva I, Lassmann H, and Turnbull D. Mitochondrial defects in
873 acute multiple sclerosis lesions. *Brain.* 2008;131(7):1722-35.
874 19. Stys PK. General mechanisms of axonal damage and its prevention. *J Neurol*
875 *Sci.* 2005;233(1-2):3-13.
876 20. Woo MS, Ufer F, Rothammer N, Di Liberto G, Binkle L, Haferkamp U, et al.
877 Neuronal metabotropic glutamate receptor 8 protects against
878 neurodegeneration in CNS inflammation. *Journal of Experimental Medicine.*
879 2021;218(5).
880 21. Schirmer L, Möbius W, Zhao C, Cruz-Herranz A, Ben Haim L, Cordano C, et
881 al. Oligodendrocyte-encoded Kir4.1 function is required for axonal integrity.
882 *eLife.* 2018;7:651.
883 22. Kelley KW, Ben Haim L, Schirmer L, Tyzack GE, Tolman M, Miller JG, et al.
884 Kir4.1-Dependent Astrocyte-Fast Motor Neuron Interactions Are Required for
885 Peak Strength. *Neuron.* 2018;98(2):306-19 e7.
886 23. Larson VA, Mironova Y, Vanderpool KG, Waisman A, Rash JE, Agarwal A, et
887 al. Oligodendrocytes control potassium accumulation in white matter and
888 seizure susceptibility. *eLife.* 2018;7:11298.
889 24. Cui Y, Yang Y, Ni Z, Dong Y, Cai G, Foncelle A, et al. Astroglial Kir4.1 in the
890 lateral habenula drives neuronal bursts in depression. *Nature.*
891 2018;554(7692):323-7.
892 25. Delmas P, and Brown DA. Pathways modulating neural KCNQ/M (Kv7)
893 potassium channels. *Nat Rev Neurosci.* 2005;6(11):850-62.

894 26. Jentsch TJ. Neuronal KCNQ potassium channels: physiology and role in
895 disease. *Nat Rev Neurosci.* 2000;1(1):21-30.
896 27. Wladyka CL, and Kunze DL. KCNQ/M-currents contribute to the resting
897 membrane potential in rat visceral sensory neurons. *J Physiol.* 2006;575(Pt
898 1):175-89.
899 28. Brown DA, and Passmore GM. Neural KCNQ (Kv7) channels. *Br J Pharmacol.*
900 2009;156(8):1185-95.
901 29. Tzingounis AV, and Nicoll RA. Contribution of KCNQ2 and KCNQ3 to the
902 medium and slow afterhyperpolarization currents. *Proceedings of the National*
903 *Academy of Sciences.* 2008;105(50):19974-9.
904 30. Devaux JJ, Kleopa KA, Cooper EC, and Scherer SS. KCNQ2 is a nodal K+
905 channel. *J Neurosci.* 2004;24(5):1236-44.
906 31. Wulff H, Castle NA, and Pardo LA. Voltage-gated potassium channels as
907 therapeutic targets. *Nat Rev Drug Discov.* 2009;8(12):982-1001.
908 32. Gunthorpe MJ, Large CH, and Sankar R. The mechanism of action of
909 retigabine (ezogabine), a first-in-class K+ channel opener for the treatment of
910 epilepsy. *Epilepsia.* 2012;53(3):412-24.
911 33. Hayashi H, Iwata M, Tsuchimori N, and Matsumoto T. Activation of peripheral
912 KCNQ channels attenuates inflammatory pain. *Mol Pain.* 2014;10:15.
913 34. Stas JI, Bocksteins E, Jensen CS, Schmitt N, and Snyders DJ. The
914 anticonvulsant retigabine suppresses neuronal KV2-mediated currents.
915 *Scientific Reports.* 2016;6(1):35080.
916 35. Large CH, Sokal DM, Nehlig A, Gunthorpe MJ, Sankar R, Crean CS, et al. The
917 spectrum of anticonvulsant efficacy of retigabine (ezogabine) in animal
918 models: implications for clinical use. *Epilepsia.* 2012;53(3):425-36.

36. Wainger BJ, Macklin EA, Vucic S, McIlduff CE, Paganoni S, Maragakis NJ, et al. Effect of Ezogabine on Cortical and Spinal Motor Neuron Excitability in Amyotrophic Lateral Sclerosis: A Randomized Clinical Trial. *JAMA Neurol.* 2020.

37. Huang W, Ke Y, Zhu J, Liu S, Cong J, Ye H, et al. TRESK channel contributes to depolarization-induced shunting inhibition and modulates epileptic seizures. *Cell Reports.* 2021;36(3):109404.

38. Porter RJ, Partiot A, Sachdeo R, Nohria V, and Alves WM. Randomized, multicenter, dose-ranging trial of retigabine for partial-onset seizures. *Neurology.* 2007;68(15):1197.

39. Brodie MJ, Lerche H, Gil-Nagel A, Elger C, Hall S, Shin P, et al. Efficacy and safety of adjunctive ezogabine (retigabine) in refractory partial epilepsy. *Neurology.* 2010;75(20):1817.

40. French JA, Abou-Khalil BW, Leroy RF, Yacubian EMT, Shin P, Hall S, et al. Randomized, double-blind, placebo-controlled trial of ezogabine (retigabine) in partial epilepsy. *Neurology.* 2011;76(18):1555.

41. D'Este E, Kamin D, Balzarotti F, and Hell SW. Ultrastructural anatomy of nodes of Ranvier in the peripheral nervous system as revealed by STED microscopy. *Proc Natl Acad Sci U S A.* 2017;114(2):E191-E9.

42. Tasic B, Yao Z, Graybuck LT, Smith KA, Nguyen TN, Bertagnolli D, et al. Shared and distinct transcriptomic cell types across neocortical areas. *Nature.* 2018;563(7729):72-8.

43. Battefeld A, Tran BT, Gavrilis J, Cooper EC, and Kole MH. Heteromeric Kv7.2/7.3 channels differentially regulate action potential initiation and conduction in neocortical myelinated axons. *J Neurosci.* 2014;34(10):3719-32.

944 44. Hansen HH, Waroux O, Seutin V, Jentsch TJ, Aznar S, and Mikkelsen JD. Kv7
945 channels: interaction with dopaminergic and serotonergic neurotransmission in
946 the CNS. *J Physiol.* 2008;586(7):1823-32.
947 45. Chung HJ, Jan YN, and Jan LY. Polarized axonal surface expression of
948 neuronal KCNQ channels is mediated by multiple signals in the KCNQ2 and
949 KCNQ3 C-terminal domains. *Proc Natl Acad Sci U S A.* 2006;103(23):8870-5.
950 46. Daldrup T, Lesting J, Meuth P, Seidenbecher T, and Pape HC. Neuronal
951 correlates of sustained fear in the anterolateral part of the bed nucleus of stria
952 terminalis. *Neurobiol Learn Mem.* 2016;131:137-46.
953 47. Moore S, Meschkat M, Ruhwedel T, Trevisiol A, Tzvetanova ID, Battefeld A, et
954 al. A role of oligodendrocytes in information processing. *Nat Commun.*
955 2020;11(1):5497.
956 48. Schroeder BC, Kubisch C, Stein V, and Jentsch TJ. Moderate loss of function
957 of cyclic-AMP-modulated KCNQ2/KCNQ3 K+ channels causes epilepsy.
958 *Nature.* 1998;396(6712):687-90.
959 49. Schirmer L, Mobius W, Zhao C, Cruz-Herranz A, Ben Haim L, Cordano C, et
960 al. Oligodendrocyte-encoded Kir4.1 function is required for axonal integrity.
961 *Elife.* 2018;7.
962 50. Jamann N, Dannehl D, Lehmann N, Wagener R, Thielemann C, Schultz C, et
963 al. Sensory input drives rapid homeostatic scaling of the axon initial segment
964 in mouse barrel cortex. *Nat Commun.* 2021;12(1):23.
965 51. Fueta Y, and Avoli M. Effects of antiepileptic drugs on 4-aminopyridine-
966 induced epileptiform activity in young and adult rat hippocampus. *Epilepsy*
967 *Res.* 1992;12(3):207-15.

52. Khalil M, Pirpamer L, Hofer E, Voortman MM, Barro C, Leppert D, et al. Serum neurofilament light levels in normal aging and their association with morphologic brain changes. *Nature Communications.* 2020;11(1):812.
53. Ridder WH, 3rd, and Nusinowitz S. The visual evoked potential in the mouse--origins and response characteristics. *Vision Res.* 2006;46(6-7):902-13.
54. Kraft GH. Evoked potentials in multiple sclerosis. *Phys Med Rehabil Clin N Am.* 2013;24(4):717-20.
55. Cruz-Herranz A, Dietrich M, Hilla AM, Yiu HH, Levin MH, Hecker C, et al. Monitoring retinal changes with optical coherence tomography predicts neuronal loss in experimental autoimmune encephalomyelitis. *J Neuroinflammation.* 2019;16(1):203.
56. Ronzano R, Roux T, Thetiot M, Aigrot MS, Richard L, Lejeune FX, et al. Microglia-neuron interaction at nodes of Ranvier depends on neuronal activity through potassium release and contributes to remyelination. *Nature Communications.* 2021;12(1):5219.
57. Coman I, Aigrot MS, Seilhean D, Reynolds R, Girault JA, Zalc B, et al. Nodal, paranodal and juxtaparanodal axonal proteins during demyelination and remyelination in multiple sclerosis. *Brain.* 2006;129(12):3186-95.
58. Moll C, Mourre C, Lazdunski M, and Ulrich J. Increase of sodium channels in demyelinated lesions of multiple sclerosis. *Brain Research.* 1991;556(2):311-6.
59. Freeman SA, Desmazières A, Fricker D, Lubetzki C, and Sol-Foulon N. Mechanisms of sodium channel clustering and its influence on axonal impulse conduction. *Cellular and Molecular Life Sciences.* 2016;73(4):723-35.
60. Prineas JW, and Connell F. Remyelination in multiple sclerosis. *Ann Neurol.* 1979;5(1):22-31.

994 61. Dietrich M, Koska V, Hecker C, Gottle P, Hilla AM, Heskamp A, et al.
995 Protective effects of 4-aminopyridine in experimental optic neuritis and multiple
996 sclerosis. *Brain.* 2020.
997 62. Administration UFaD. FDA labeling information — Potiga.
998 https://www.accessdata.fda.gov/drugsatfda_docs/label/2011/022345s000lbl.p
999 df. Accessed November 28, 2022.
1000 63. (EMA) EMA. European Public Assessment Report — Trobalt.
1001 https://www.ema.europa.eu/en/documents/product-information/trobalt-epar-
1002 product-information_en.pdf. Accessed November 28, 2022.
1003 64. Lappe-Siefke C, Goebbels S, Gravel M, Nicksch E, Lee J, Braun PE, et al.
1004 Disruption of Cnp1 uncouples oligodendroglial functions in axonal support and
1005 myelination. *Nat Genet.* 2003;33(3):366-74.
1006 65. Djukic B, Casper KB, Philpot BD, Chin LS, and McCarthy KD. Conditional
1007 knock-out of Kir4.1 leads to glial membrane depolarization, inhibition of
1008 potassium and glutamate uptake, and enhanced short-term synaptic
1009 potentiation. *J Neurosci.* 2007;27(42):11354-65.
1010 66. Schüller U, Heine VM, Mao J, Kho AT, Dillon AK, Han YG, et al. Acquisition of
1011 granule neuron precursor identity is a critical determinant of progenitor cell
1012 competence to form Shh-induced medulloblastoma. *Cancer Cell.*
1013 2008;14(2):123-34.
1014 67. Schütze S, Orozco IJ, and Jentsch TJ. KCNQ Potassium Channels Modulate
1015 Sensitivity of Skin Down-hair (D-hair) Mechanoreceptors. *J Biol Chem.*
1016 2016;291(11):5566-75.
1017 68. Gao X, Bender F, Soh H, Chen C, Altafi M, Schütze S, et al. Place fields of
1018 single spikes in hippocampus involve Kcnq3 channel-dependent entrainment
1019 of complex spike bursts. *Nature Communications.* 2021;12(1):4801.

69. Velmeshev D, Schirmer L, Jung D, Haeussler M, Perez Y, Mayer S, et al. Single-cell genomics identifies cell type-specific molecular changes in autism. *Science.* 2019;364(6441):685-+.

70. Stuart T, Butler A, Hoffman P, Hafemeister C, Papalexi E, Mauck WM, 3rd, et al. Comprehensive Integration of Single-Cell Data. *Cell.* 2019;177(7):1888-902.e21.

71. Trapnell C, Cacchiarelli D, Grimsby J, Pokharel P, Li S, Morse M, et al. The dynamics and regulators of cell fate decisions are revealed by pseudotemporal ordering of single cells. *Nature Biotechnology.* 2014;32(4):381-6.

72. Haghverdi L, Lun ATL, Morgan MD, and Marioni JC. Batch effects in single-cell RNA-sequencing data are corrected by matching mutual nearest neighbors. *Nature Biotechnology.* 2018;36(5):421-7.

73. Zhang Y, Pak C, Han Y, Ahlenius H, Zhang Z, Chanda S, et al. Rapid single-step induction of functional neurons from human pluripotent stem cells. *Neuron.* 2013;78(5):785-98.

74. Mei F, Lehmann-Horn K, Shen YA, Rankin KA, Stebbins KJ, Lorrain DS, et al. Accelerated remyelination during inflammatory demyelination prevents axonal loss and improves functional recovery. *Elife.* 2016;5.

75. Gobel K, Wedell JH, Herrmann AM, Wachsmuth L, Pankratz S, Bittner S, et al. 4-Aminopyridine ameliorates mobility but not disease course in an animal model of multiple sclerosis. *Exp Neurol.* 2013;248:62-71.

76. Nodera H, Spieker A, Sung M, and Rutkove S. Neuroprotective effects of Kv7 channel agonist, retigabine, for cisplatin-induced peripheral neuropathy. *Neurosci Lett.* 2011;505(3):223-7.

77. Ihara Y, Tomonoh Y, Deshimaru M, Zhang B, Uchida T, Ishii A, et al. Retigabine, a Kv7.2/Kv7.3-Channel Opener, Attenuates Drug-Induced

Seizures in Knock-In Mice Harboring Kcnq2 Mutations. *PLoS One.* 2016;11(2):e0150095.

78. Kalappa BI, Soh H, Duignan KM, Furuya T, Edwards S, Tzingounis AV, et al. Potent KCNQ2/3-specific channel activator suppresses in vivo epileptic activity and prevents the development of tinnitus. *J Neurosci.* 2015;35(23):8829-42.

Figures and legends

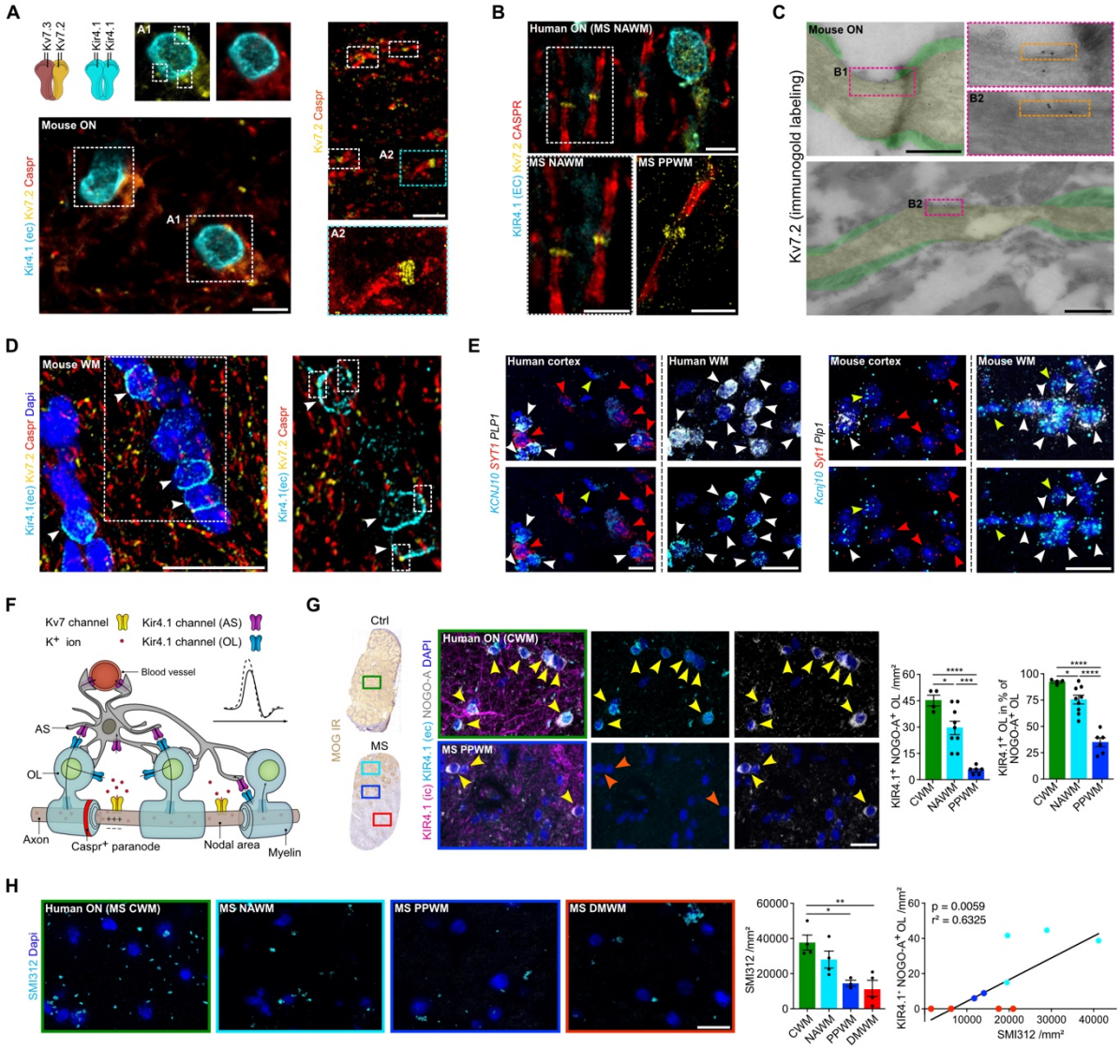

Figure 1. Investigation of Kir4.1 and Kv7 channels in neuroglial cell types under homeostatic and inflammatory-demyelinating conditions. (**A, B**) Triple staining (Caspr, Kir4.1 [extracellular epitope, EC], Kv7.2) reveals a specific nodal expression of Kv7.2 (flanked by Caspr IR) adjacent to OL-Kir4.1 channel IR in mouse (**A**) and human (**B**) ON. A2 closeup (STED image) shows the ~190 nm periodic organization of Kv7.2. (**C**) Kv7.2 immunogold electron microscopy labeling shows presence of gold particles in nodal areas (yellow) between myelin sheets (green) in control mouse ON. (**D**) Triple staining (cf Figure 1A) confirms juxtapositioning of OL-Kir4.1 and nodal Kv7.2 channels (white arrows) in other mouse WM tracts (corpus callosum). (**E**) Perineuronal

Kcnj10/KCNJ10 expression (ISH) is visualized in mouse/human cortex with *Plp1*$^{+}$/*PLP1*$^{+}$ and *Kcnj10*$^{+}$/*KCNJ10*$^{+}$ co-expressing OLs (white arrows) next to *Syt1*$^{+}$/*SYT1*$^{+}$ and *Kcnj10*$^{-}$/*KCNJ10*$^{-}$ neurons (red arrows). Yellow arrows indicate *Kcnj10*$^{+}$/*KCNJ10*$^{+}$ *Plp1*$^{-}$/*PLP1*$^{-}$ astrocytes. (**F**) Cartoon illustrates neuron-OL for K^{+} shuttling mechanism: neuronal Kv7 channels mediate axonal K^{+} efflux and OL-Kir4.1 channels mediate extracellular K^{+} uptake and siphoning through interaction with astrocyte Kir4.1 channels. (**G**) In human MS ON, KIR4.1 channel IR (antibodies against intracellular [specific for OL-KIR4.1 and AS-KIR4.1] and extracellular [specific for OL-KIR4.1] epitopes) is preserved on AS fibers in lesions. OL-KIR4.1 channel IR (yellow arrows) is reduced in MS NAWM areas (n = 9) and lost in PPWM (n = 6) relative to CWM (n = 4) based on MOG IR. (**H**) SMI312^{+} axon density is gradually lost in MS ON tissues toward the lesion rim and correlates with OL-KIR4.1 channel loss. Scale bars: (**A**, **B**) 5 µm; (**C**) 0.5 µm; (**D**, **E**, **G**) 20 µm; (**H**) 100 µm. (**G**) One-way ANOVA; (**H**) One-way ANOVA (left), simple linear regression (right).

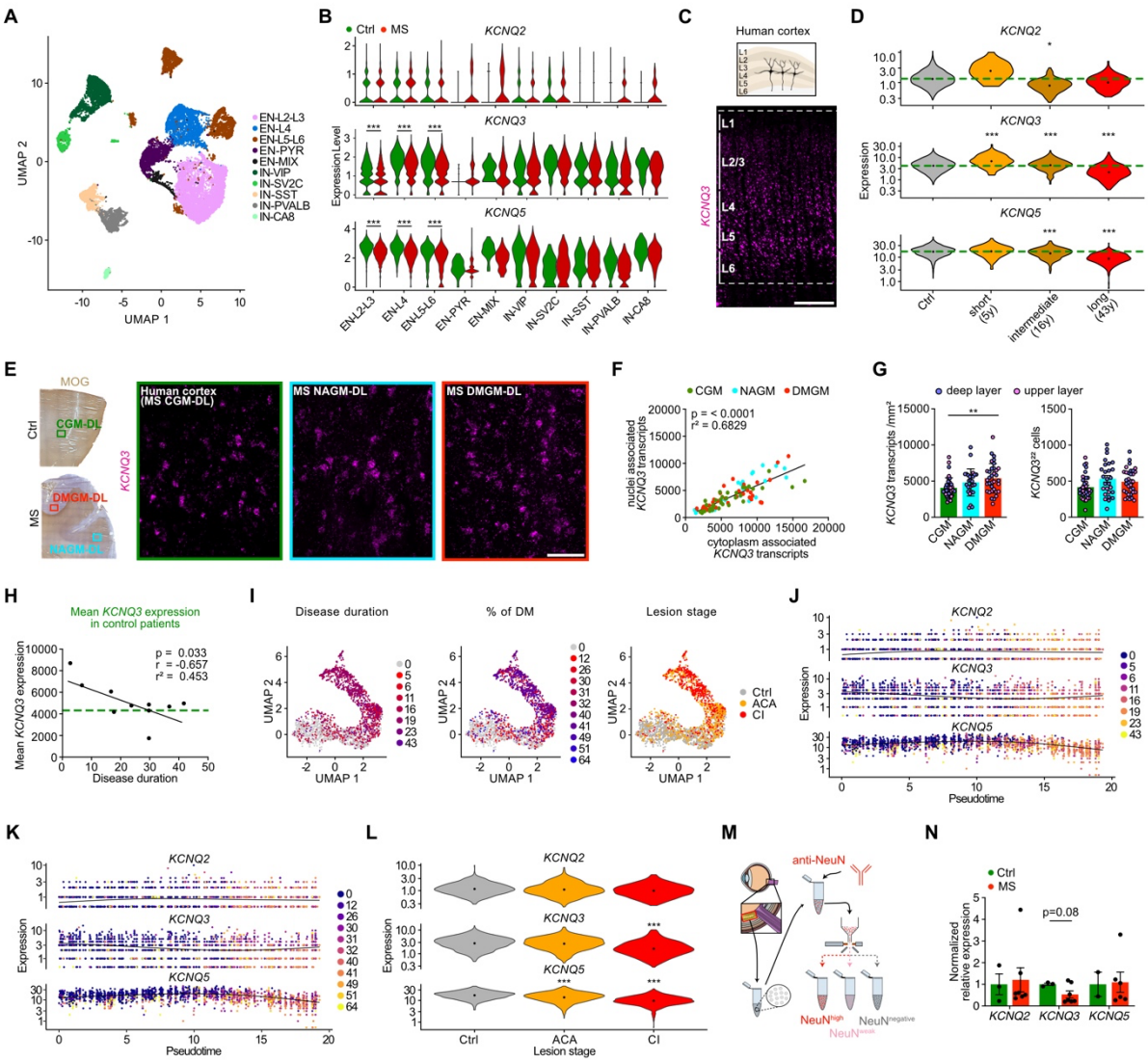

Figure 2. *KCNQ*3 dysregulation in cortical and retinal MS tissues. (**A**) UMAP plot visualizes clustering of human excitatory (EN) and inhibitory (IN) cortical neurons based on published snRNA-seq dataset (12). (**B**) Normalized *KCNQ2/-3/-5* expression in control and MS human cortical neurons. (**C**) Spatial *KCNQ3* expression (ISH) in the human cortex. (**D**) Violin plots visualize average *KCNQ2/-3/-5* expression (snRNA-seq, **A**) in control neurons (n = 5; green dashed line) and representative MS samples from patients with various disease duration. (**E**) *KCNQ3* ISH in human CGM and MS NAGM and DMGM lesion areas based on MOG IR. UL: upper layers: DL: deep (**F**) Correlation of nucleus- and cytoplasm-associated *KCNQ3* transcript counts within the same cell in human cortical tissues (ISH) quantification in CGM (n = 35 areas, 5

patients), NAGM (n = 27 areas, 8 patients) and DMGM (n = 34 areas, 8 patients). (**G**) *KCNQ3* upregulation in DMGM (ISH) independent of neuronal density. (**H**) Gradual loss of mean *KCNQ3* expression in MS GM tissues (ISH) with prolonged MS disease duration approaching CGM expression levels (n = 5, green dashed line). (**I**) Unsupervised trajectory inference of upper L2/3 neuron branch and nuclei distribution along the trajectory (cf. Figure S3E,F) based on MS disease duration, demyelination extent and lesion stage. ACA: acute chronic active, CI: chronic inactive. (**J, K**) Pseudotime-dependent *KCNQ2/-3/-5* expression in relation to disease duration and demyelination based on MOG IR. (**L**) Neuronal *KCNQ2/-3/-5* expression grouped by lesion stage. (**M**) Sorting of retinal nuclei based on NeuN IR. (**N**) Normalized *KCNQ2/-3/-5* expression (qPCR) in human RGC nuclei (controls: n = 6; MS: n = 7). Scale bars: (**C**) 500 µm; (**E**) 100 µm. (**B**) Wilcoxon rank sum test, Bonferroni correction; (**D**, **L**) Generalized linear model, Wald test, Benjamini and Hochberg correction; (**F**, **H**) Simple linear regression; (**G**) Kruskal-Wallis; (**N**) Mixed-effects model with Geisser-Greenhouse correction and Sidak's multiple comparison test.

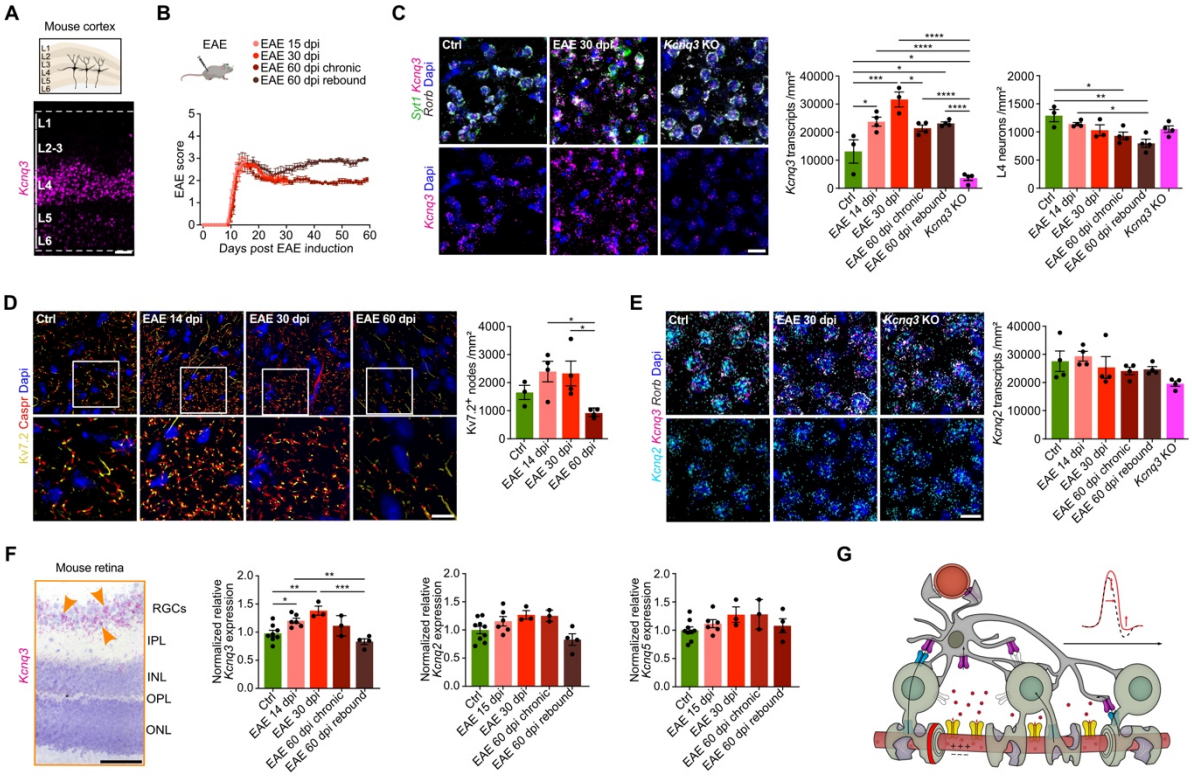

Figure 3. Dysregulation of Kv7 subunits in cortical and retinal EAE tissues. (**A**) Spatial *Kcnq3* expression (ISH) in the mouse cortex. (**B**) Overview plot visualizes different EAE groups including endpoints at 15, 30 and 60 dpi; note chronic EAE groups (endpoint at 60 dpi) were divided into two groups separating animals with/without clinical worsening (rebound). (**C**) *Kcnq3* expression (ISH) in *Syt1*$^{+}$ *Rorb*$^{+}$ L4 mouse neurons at 14, 30 and 60 dpi in EAE (each n = 4) and controls (n = 3); *Kcnq3* KO mouse tissue shows strong reduction in *Kcnq3* expression (n = 4). (**D**) Density of Kv7.2^{+} nodes (framed by Caspr^{+} IR) based on IR in L4 cortical areas at 14, 30 and 60 dpi in EAE (each n = 4) and controls (n = 3). (**E**) *Kcnq2* expression based on ISH in L4 mouse neurons at at 14, 30 and 60 dpi in EAE, controls and and *Kcnq3* KO (each n = 4). (**F**) *Kcnq3* expression (ISH) of mouse retinal speciments comprising inner plexiform layer (IPL), inner nuclear layer (INL), outer plexiform layer (OPL) and outer nuclear layer (ONL) reveals specific *Kcnq3* expression in RGCs (yellow arrows). Normalized *Kcnq2/3/5* expression (qPCR) in sorted mouse NeuN^{high} RGC nuclei (control: n = 9; 15

dpi: n = 6; 30 dpi: n = 3, 60 dpi chronic: n = 3; 60 dpi rebound: n = 4). (**G**) Cartoon illustrates dysregulated neuron-OL K^+ shuttling during inflammatory demyelination resulting in neuronal hyperexcitability, axonal swelling and impaired neuronal function in addition to OL-Kir4.1 loss (colorless channels with dashed borders) and transient upregulation of nodal Kv7 channels. Scale bars: (**A**, **F**) 100 μm; (**C**-**E**) 20 μm. (**C**-**F**) One-way ANOVA.

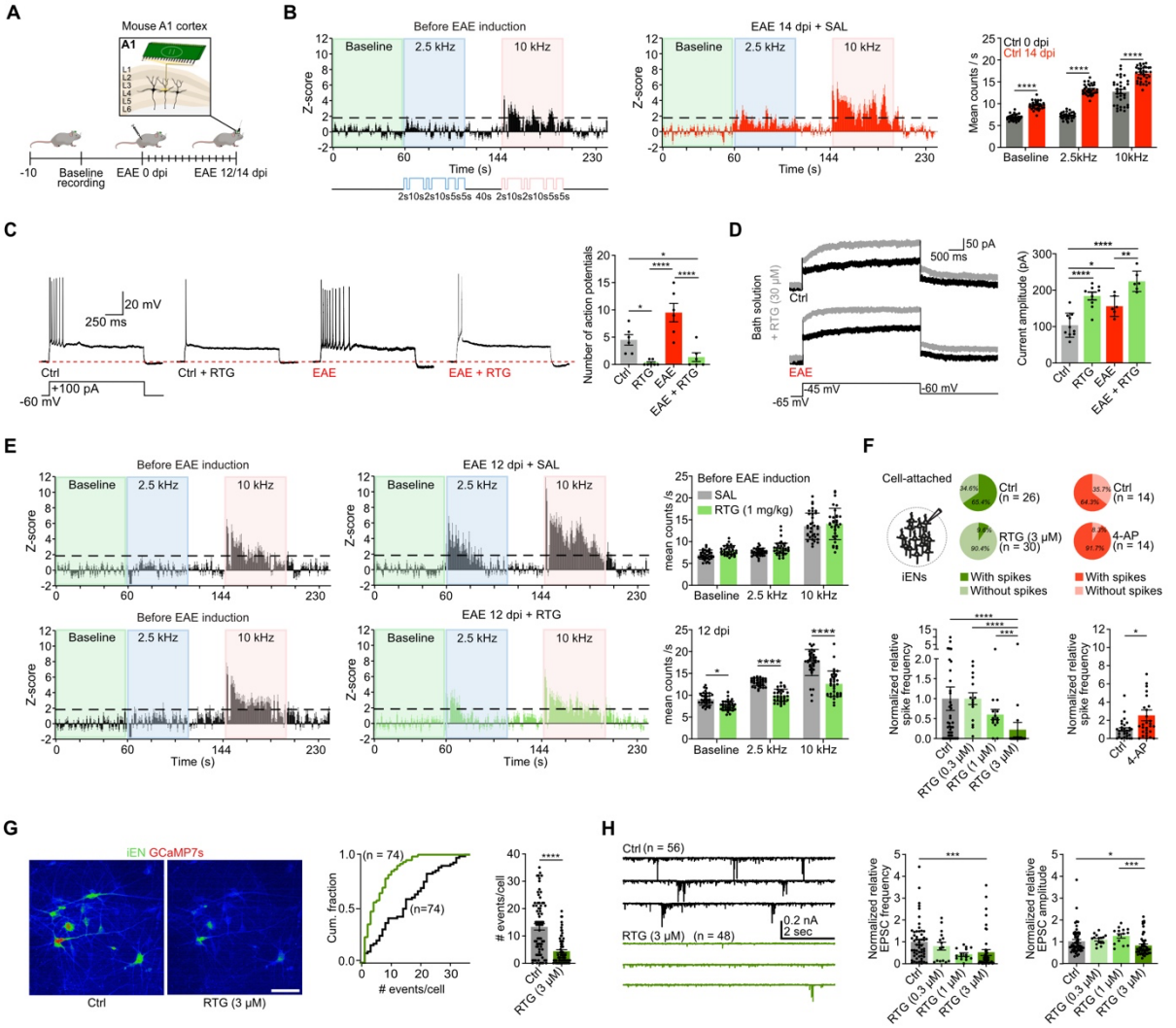

Figure 4. Altered neuronal excitability and network activity in EAE. (**A**) Cartoon illustrates *in vivo* recordings from mouse primary auditory cortex (A1). (**B**) Z-score analysis of mouse auditory neurons before EAE induction demonstrates a tonotopic organization of the auditory cortex with neuronal response to 10 kHz (pink insets) but not 2.5 kHz (blue insets) tones relative to baseline (green insets). EAE induction augments overall neuronal activity and disrupts tonotopic organization (increased neuronal response to 2.5 kHz) (each n= 34). (**C, D**) RTG (30 µM) reduces neuronal excitability (**C**) and increases M-currents (**D**) in control (**C**, untreated: n = 6, RTG: n = 7; **D**, untreated: n = 10, RTG: n = 9) and 12 dpi EAE (each n = 6) mouse brain sections. (**E**) Continuous RTG treatment (1 mg/kg) starting at baseline prevents EAE-associated

increase in neuronal excitability at 12 dpi (lower panel, right) resulting in similar z-scores before EAE induction (left panels) (each n = 34). (**F**) RTG (0.3 µM, n = 15; 1 µM, n = 15; 3 µM, n = 30) reduces normalized relative iEN firing in a dose-dependent manner compared to untreated iENs (n = 41). Kv channel blocker 4-AP increases spontaneous firing (each n = 29). (**G**) GCaMP7s-reporter iENs show reduced spontaneous calcium transients in response to RTG (3 µM, each n = 74). (**H**) Representative EPSC traces reveal reduced normalized relative EPSC frequency and amplitudes (0.3 µM, n = 15; 1 µM, n = 14 (amplitude), 15 (frequency); 3 µM, n = 48) of RTG-treated iENs in a dose-dependent manner compared to controls (frequency: n = 56; amplitude: n = 55). Scale bars: (**G**) 80 µm. (**B**) Two-way ANOVA; (**C**, **D**) One-way ANOVA; (**E**) Multiple unpaired t-tests; (**F**) Kruskal-Wallis (left), Mann-Whitney (right); (**G**) Two-way ANOVA (left), Mann-Whitney (right); (**H**) Kruskal-Wallis.

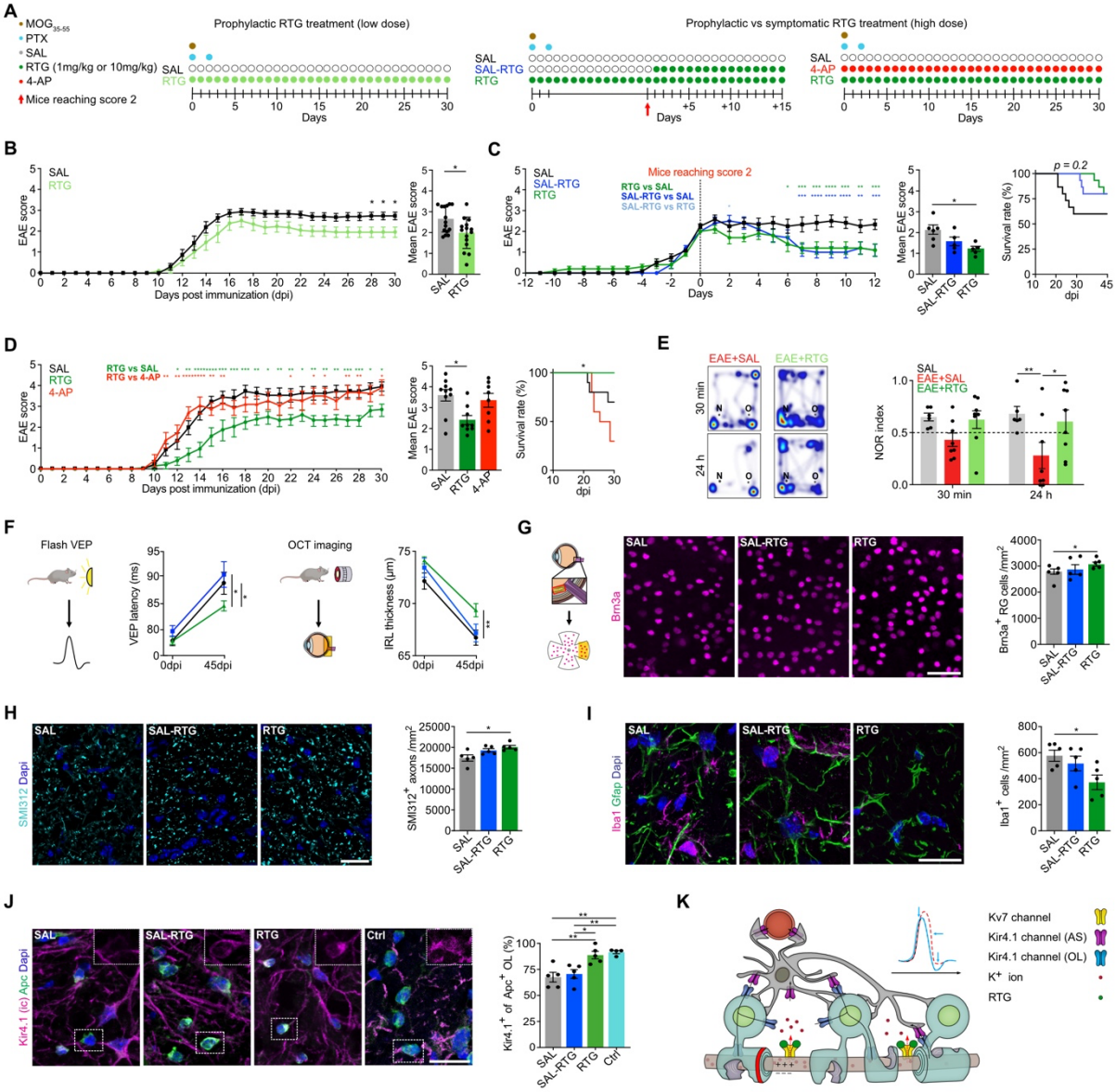

Figure 5. Neuroprotective effects of RTG on structural and functional levels. (**A**) Illutstration shows different RTG treatment regimes. (**B**) Prophylactic low-dose RTG treatment (1 mg/kg) attenuates motor deficits in chronic EAE (each n = 15). (**C**) Prophylactic and symptomatic (starting at EAE score ≥ 2) high-dose RTG treatment (10 mg/kg, both n = 5) attenuates EAE courses compared to SAL-treated controls (n = 6); note only prophylactic RTG treatment increases survival. (**D**) High-dose RTG treatment (n = 9) attenuates early EAE progression and increases survival relative to controls (n = 10). 4-AP treatment increases mortality (n = 8). (**E**) Memory function decline in SAL-treated EAE that is prevented by RTG treatment (each n = 8) compared

to non-EAE mice (n = 6) in NOR testing 24 hours after habituation (dashed line indicates threshold for memory impairment). (**F**) OCT imaging (45 dpi EAE) shows thinning of inner retinal layers in SAL-treated mice (n = 18) that is prevented by prophylactic (n = 22) but not symptomatic (n = 9) RTG treatment. VEP latency delay (45 dpi EAE) is improved by prophylactic (n = 11) but not symptomatic (n = 5) RTG treatment compared to SAL-treated mice (n = 7). (**G**-**I**) Only prophylactic but not symptomatic RTG treatment prevents loss of Brn3a$^+$ RGCs (**G**) and SMI312$^+$ ON axons (**H**) and decreases Iba1$^+$ cell infiltration (**I**) in EAE mice at 45 dpi (each n = 5). (**J**) Also, only prophylactic but not symptomatic RTG treatment prevents OL-Kir4.1 channel loss at 45 dpi in EAE (each n = 5) maintaining similar levels to non-EAE controls (n = 4). (**K**) Cartoon illustrates neuron-OL for K^+ shuttling mechanism during inflammatory demyelination: Enhanced (transient) neuronal Kv7 channel function augments axonal K^+ efflux, counteracting neuronal hyperexcitability and contributing to neuroprotection and preservation of OL-Kir4.1 function. Scale bars: (**G**) 50 µm; (**H**-**J**) 20 µm. (**B**) Mixed-effects analysis with multiple comparisons (left), Mann-Whitney (right); (**C**, **D**) Two-way ANOVA (left), Kruskal-Wallis (middle), Mantel-Cox (right); (**E**, **F**) Two-way ANOVA; (**G**-**J**) One-way ANOVA.

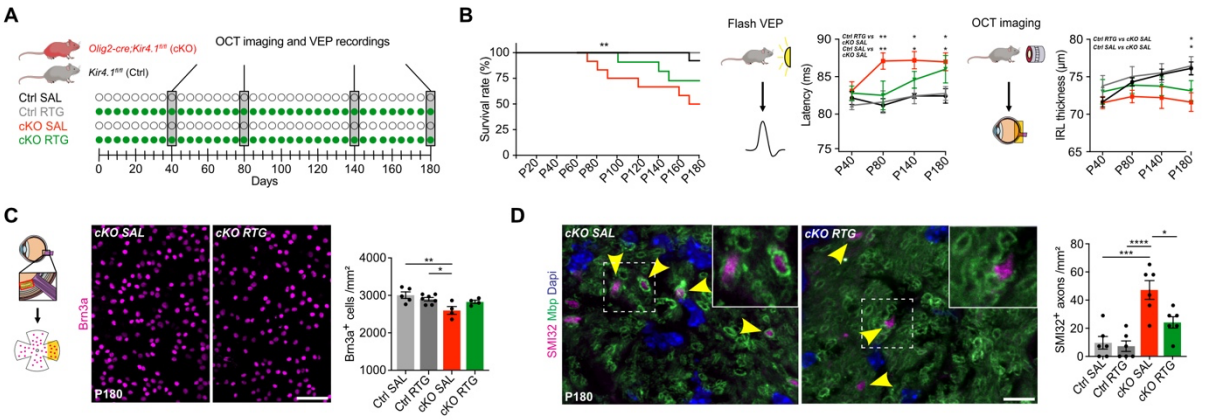

Figure 6. Effects of chronic RTG treatment in OL-*Kcnj10* deficient mice. (**A**) Scheme of continuous RTG versus SAL treatment in OL-*Kcnj10* KO mice versus controls. (**B**) Chronic RTG treatment increases survival in both control (SAL, n = 13; RTG, n = 12) and OL-*Kcnj10* KO (SAL, n = 12; RTG, n = 11) animals at P180. Delayed VEP latencies in SAL- but not RTG-treated (both n = 5) OL-*Kcnj10* KO versus SAL- (n = 9) RTG-treated (n = 8) animals at P80; note delayed VEP latencies with aging in both SAL- and RTG-treated KO groups at P140 and P180. IRLs show physiological growth during aging in both SAL- and RTG-treated (both n = 8) control and RTG-treated but not SAL-treated (both n = 5) OL-*Kcnj10* KO animals until P140. At P180, IRL thinning occurs only in SAL- but not RTG-treated KO mice. (**C**) Chronic RTG treatment (n = 4) prevents loss of Brn3a$^+$ RGCs in SAL-treated (n = 5) OL-*Kcnj10* KO mice compared to SAL- (n = 5) and RTG-treated (n = 7) controls. (**D**) RTG treatment prevents increased counts of dystrophic/damaged SMI32$^+$ axons in the ON as seen in SAL-treated OL-*Kcnj10* KO mice compared to controls (n = 6 for each group). Scale bars: (**C**) 20 µm; (**D**) 10 µm. (**B**) Mantel-Cox (left), two-way ANOVA (right, VEP and OCT); (**C**, **D**) One-way ANOVA.